

UC Irvine

UC Irvine Electronic Theses and Dissertations

Title

Optimized Experimental Observation and Measurements of Pool Boiling Heat Transfer Using Computer Vision Techniques

Permalink

<https://escholarship.org/uc/item/0qj8j96h>

Author

Lee, Marissa

Publication Date

2022

Peer reviewed|Thesis/dissertation

UNIVERSITY OF CALIFORNIA, IRVINE

Optimized Experimental Observation and Measurements of Pool Boiling Heat Transfer
Using Computer Vision Techniques

THESIS

Submitted in partial satisfaction of the requirements for the degree of

MASTER OF SCIENCE

In Mechanical and Aerospace Engineering

by

Marissa Lee

Thesis Committee:

Professor Yoonjin Won, Chair

Professor Yun Wang

Professor Penghui Cao

2022

TABLE OF CONTENTS

	Page
LIST OF FIGURES	iv
LIST OF TABLES	vi
ACKNOWLEDGMENTS	vii
ABSTRACT OF THESIS	viii
CHAPTER 1: INTRODUCTION	1
1.1 Two-Phase Heat Management Motivation	1
1.2 Fundamentals of Pool Boiling	3
1.2.1 Definition	3
1.2.2 Pool Boiling Interactions	3
1.2.3 Performance Modeling	5
1.3.1 Heat Transfer Enhancement Techniques	9
1.3.2 Bubble Dynamics	11
1.3.3 Heat Transfer Prediction Methods	18
1.4 Thesis Objectives	20
CHAPTER 2: COMPUTER VISION MODEL	22
2.2 Model Framework	25
2.3 Mask R-CNN Training	26
2.4 Feature Extraction	28
2.5 Model Validation	28
CHAPTER 3: OPTIMIZED POOL BOILING SETUP	30
3.1 Structural design	30
3.2 Vendor Search	39
3.3 Subsystems Design	43
3.3.1 Reflux System	43
3.3.2 Heating Source System	44
3.3.3 Temperature Acquisition System	46
3.3.4 Visualization System	48
3.4 Final Setup Assembly	49
CHAPTER 4: EXPERIMENTAL METHODOLOGY	51
4.1 Sample Preparation	51
4.2 Sample Mounting	51
4.3 Setup Preparation and Clean up	53
4.4 Image Acquisition	53
4.5 Thermal Measurement	54

4.6 Heat Flux Prediction Using Bubble Statistics	56
CHAPTER 5: SUMMARY AND CONCLUSION	58
REFERENCES	59

LIST OF FIGURES

	Page
Figure 1: Attainable heat transfer coefficients for various cooling schemes	2
Figure 2: Pool boiling curve of water at atmospheric pressure	4
Figure 3: Ideal pool boiling curves	7
Figure 4: Optimum pool boiling curve for temperature sensitive devices	8
Figure 5: Comparison of bubble departure diameter prediction models	13
Figure 6: Computer vision model framework flowchart including the object detection module, object tracking module, data processed module	26
Figure 7: Supervisely annotation of pool boiling image (a) original image 27(b) annotated image	27
Figure 8: Model performance metric for validation	29
Figure 9: Liquid chamber design	31
Figure 10: Rubber gasket design	31
Figure 11: Elevated heated surface	32
Figure 12: Heating block design	33
Figure 13: Heating block dimensions	33
Figure 14: Schematic of heat transfer from heating block to air/teflon	34
Figure 15: Teflon and air thermal performance comparison (a) Thermal resistance plot (b) Heat transfer plot	35
Figure 16: Upper base design	36
Figure 17: Side view of thermocouple hole alignment	36
Figure 18: Lower base design	37
Figure 19: Lid design	38
Figure 20: Lid assembly design	38
Figure 21: Pool boiling setup design assembly	39
Figure 22: Additional machining tool purchases (a) 10mm square broach (b) #51 extra long drill bit	41

Figure 23: Reflux condenser(24/40 Dimroth Condenser, Laboy Inc.)	44
Figure 24: Water pump(3 Speed Circulation Pump, Tysun Inc.)	44
Figure 25: Cartridge heater(CIR-20191/120V, Omega Inc.)	45
Figure 26: Immersion heater(120V portable water heater, Lewis N. Clark Inc.)	45
Figure 27: AC power supply(Bench Top 20 Amp Variac Variable Auto-Transformer)	46
Figure 28: (a) PID controller(100V-220V Digital Thermostat Temperature PID Controller, Inkbird Inc.) (b) Solid state relay(40A SSR, Inkbird Inc.)	46
Figure 29: K-type thermocouple(TJ36-CASS-116U-6, Omega Inc.)	47
Figure 30: USB data acquisition system(U6, LabJack Inc.)	47
Figure 31: High speed camera(Mini AX50, FAST CAM Inc.)	48
Figure 32: Adjustable light source (SugarCUBE LED fiber optic, The Ushio America Inc.)	48
Figure 33: Pool boiling experimental setup components	49
Figure 34: Schematic of pool boiling experimental setup	50
Figure 35: Sample mounting (a) 90° cross-locking tweezers (b) Mounting method Illustration	52
Figure 36: Obscured visualization from outer edge bubble nucleation	52
Figure 37: Schematic cross section of heating block fin with mounted sample	55

LIST OF TABLES

	Page
Table 1: Material and fabrication vendor trade study	40
Table 2: UC Irvine machine shop estimates	41
Table 3: Material vendor trade study	42

ACKNOWLEDGMENTS

I would like to express my deepest appreciation to my committee chair, Professor Yoonjin Won, who gave me the opportunity to research two-phase heat transfer within her group. She ultimately inspired me to pursue an education and career in thermal sciences and without her guidance and encouragement, this project would not have been possible.

I would also like to acknowledge Youngjoon Suh for his continuous help throughout this research project. I greatly appreciate the time and effort he put into improving my knowledge on pool boiling physics and machine learning-based computer vision.

And most of all, I would like to thank my parents for their unconditional support through everything and anything I endeavor in.

ABSTRACT OF THESIS

Optimized Experimental Observation and Measurements of Pool Boiling Heat Transfer
Using Computer Vision Techniques

By

Marissa Lee

Master of Science in Mechanical and Aerospace Engineering

University of California, Irvine, 2022

Assistant Professor Yoonjin Won, Chair

With power dissipation rates of modern technologies on the rise, enormous efforts are going toward leveraging one of nature's most effective thermal management mechanisms, known as boiling. In this endeavor, researchers have come to recognize the potential of visual data as it can provide real-time bubble characteristics in relation to the boiling heat flux. Key parameters to existing heat transfer performance models are nucleation site density, bubble departure diameter and bubble departure frequency. Although boiling images are richly embedded with these bubble statistics, conventional methods of extracting and analyzing such data is laborious and requires extensive user involvement. This potentially introduces errors, producing simplified and unrealistic prediction models that ultimately muddle our understanding of boiling processes. Although recent advancements in machine learning have enabled more efficient ways of processing data to classify boiling characteristics, there have been very few efforts in using image-based machine learning methods (i.e., computer vision) to correlate bubble dynamics with heat transfer performance. Such contributions of detailed data can be exploited to refine the existing, weak, theoretical models. Therefore, this study seeks to address these challenges and aid in the efforts of understanding the fundamental physics governing pool boiling through visualization techniques. We present a state of the art experimental setup and procedure that can be integrated into other laboratories as well as applied to various pool boiling experiments

studying differing conditions(e.g., enhanced surfaces or fluids). Our optimized pool boiling setup is designed and fabricated to ensure excellent structural integrity, thermal insulation, and system efficiency all while allowing easy and accurate image and thermal data acquisition. This setup works in tandem with our machine learning-based computer vision model that is capable of autonomously capturing a large bandwidth of spatio-temporal bubble statistics and quantifying heat transfer performance from high-resolution boiling images. Overall, our experimental methodology and non-invasive vision-based approach to studying pool boiling dynamics, gives rise to improved heat transfer performance to progress efforts in managing thermal dissipation of high-power devices.

CHAPTER 1: INTRODUCTION

The applications for pool boiling are immense as it has been proven to be one of nature's most effective methods of heat transfer. This mechanism is used to manage the increasing heat generation of high performance systems and can be found in essentially all modern industries. With the arousing rate of technological advancements, researchers are constantly and extensively evaluating new phase-change cooling schemes to provide a means to simpler yet more efficient thermal management designs. Approaches to analyze the performance of these phase change systems are also vast. The fusing of visual data and recent developments in machine learning have enabled researchers to explore more efficient and accurate techniques to understand as well as predict boiling physics. Although the major parameters that affect pool boiling heat transfer have been well studied, such advancements have opened the door to gaining new insight into this highly complex phenomenon. This chapter will further dive into the fundamentals of pool boiling and its evolving potential in the realm of thermal management.

1.1 Two-Phase Heat Management Motivation

Rapid development in computing capabilities has brought on the challenge of exponential growth in power dissipation. As the ability to maintain desirable operating temperature is a critical factor in system performance and reliability, scientists and engineers are constantly seeking ways to improve cooling technologies [1]. The most common schemes used to dissipate thermal energy in the electronics industry involve natural convection or single phase forced convection. Natural convection, typically executed with heat sinks, utilizes differences in fluid density along a temperature gradient to induce fluid motion while single phase forced convection achieves this motion using an external source such as a fan or pump. However, these methods have their limitations when it comes to higher power devices that require high heat fluxes accompanied with low surface temperatures. For instance, the miniaturization of

electronics and power devices in the mid 1980s pushed cooling heat flux requirements to surpass $10^2 W/cm^2$ and have now soared to an ultra-high-flux range of $10^3 - 10^5 W/cm^2$ [2].

This steepening trend in heat dissipation rates of cutting-edge technologies has led to the emergence of a more efficient and effective thermal management technique called two-phase cooling. The process involves the removal of sensible as well as latent heat through evaporation or condensation of a working fluid. Figure 1 illustrates the various cooling schemes with their corresponding attainable heat transfer coefficients. As conveyed, boiling two-phase flow holds superior cooling performance, achieving heat transfer coefficients an order of magnitude greater than natural convection or single phase forced convection [2].

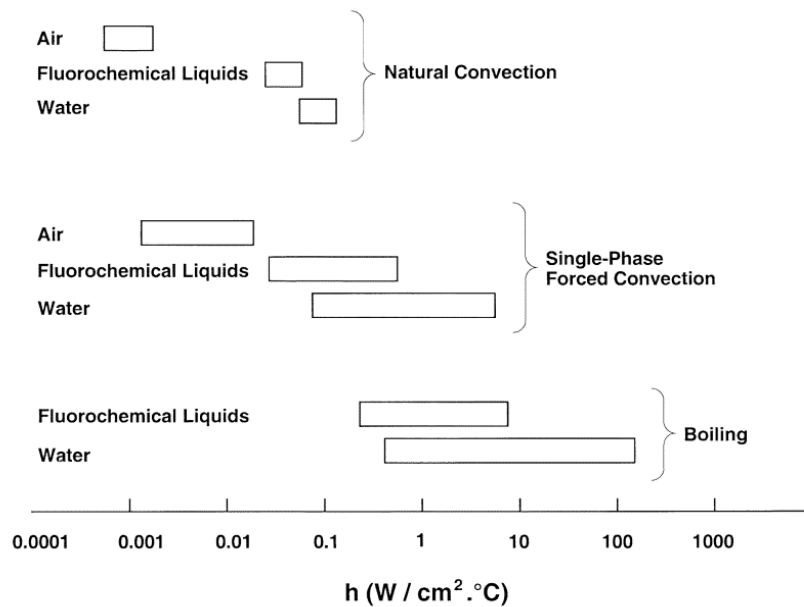


Figure 1: Attainable heat transfer coefficients for various cooling schemes [2]

Consequently, two-phase change processes are now greatly embedded and prevalent in modern technologies. Some high temperature applications include air-fuel heat exchangers for aircraft engines, fusion reactor blankets, particle accelerator targets, magnetohydrodynamic electrode walls and rocket nozzles [3]. Some low temperature applications are nuclear reactors,

computer data centers, electric vehicle power electronics, aircraft and spacecraft avionics, laser and microwave directed energy weapon electronics, advanced radars, X-ray medical devices, and turbine engines [3].

1.2 Fundamentals of Pool Boiling

1.2.1 Definition

Boiling is simply known as the two-phase change process of liquid to vapor. It occurs at the solid-liquid interface when the temperature of the solid surface (T_s) is sufficiently higher than the saturation temperature of the liquid (T_{sat}) [4]. This corresponds to Newton's law of cooling which is the following expression [5]:

$$q_s'' = h(T_s - T_{sat}) = h\Delta T_e \quad (1)$$

When heat transfers from the solid to liquid, evaporation occurs where some of the heated liquid is turned into vapor. This results in the formation of bubbles, columns or films that pull away from the surface, inherently cooling it. With natural convection or pool boiling, this occurs through buoyant forces whereas with mixed convection or flow boiling, this results from a combination of buoyant forces and a forced flow. In this study, we will be focusing on only pool boiling. In pool boiling, this phenomenon can also be categorized by whether it is subcooled or saturated. Subcooled boiling takes place when the liquid temperature is below the saturation temperature where vapor recondenses before it reaches the free surface. If the temperature of the liquid is greater than the saturation temperature, the bubbles formed at the heated surface will rise to the free surface, meaning all the liquid is saturated.

1.2.2 Pool Boiling Interactions

Boiling requires the liquid adjacent to the surface to be superheated above the liquid's saturation temperature. As the superheat increases with higher heat flux, more bubbles begin to form and

depart from the surface, drawing in more bulk liquid. This process is then repeated and new bubbles begin to form, replacing the ones just released. The surface cools as vapor is pulled away; however, as the dynamics of the vapor bubble formation affects the motion of liquid near the surface, it also has a significant impact on the amount of heat transferred [5]. The best way to understand pool boiling heat transfer is to refer to a pool boiling curve that was first discovered by S. Nukiyama in 1934. Nukiyama identified most boiling regimes in his power-controlled heating study conducted with a horizontal, metal wire submerged in water [5]. However, the pool boiling curve in figure 2 represents a temperature-controlled experiment of water at atmospheric pressure, that therefore achieves the transition boiling regime.

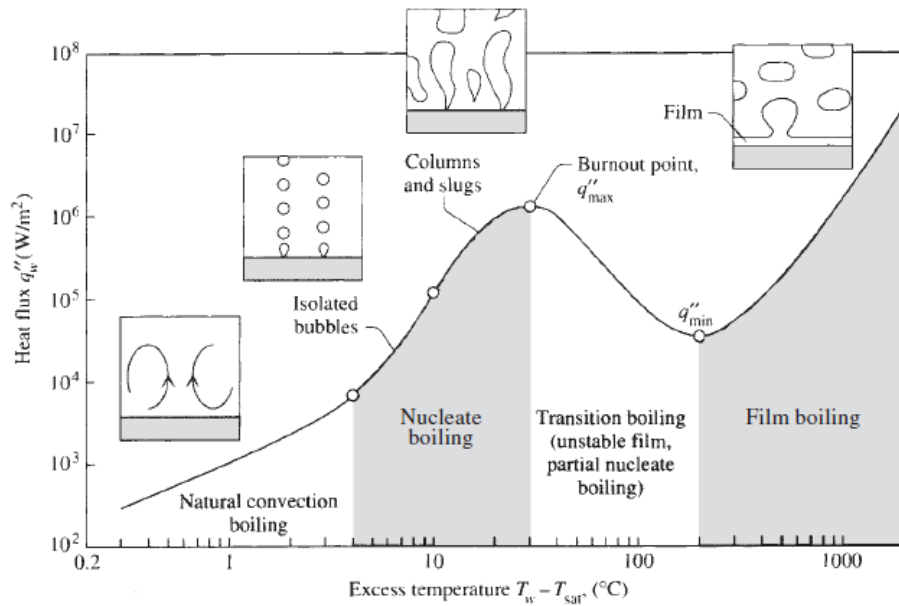


Figure 2: Pool boiling curve of water at atmospheric pressure [4]

The boiling curve represents the relationship between heat flux(q_s'') and the excess temperature (T_e) of water at atmospheric pressure with the slope as the heat transfer coefficient(HTC). It is separated into four different regimes that correspond to differing bubble dynamics. In the first regime, at very low excess temperatures, natural convection occurs where heat transfers without bubbles. During this process, non-condensable vapor is trapped in cavities, or

nucleation sites, on the heated surface and as heat is applied to this surface, a superheated liquid layer is formed. With enough heat, vapor bubbles will grow in this superheated liquid layer until they depart, scavenging away the superheated layer. Simultaneously, cold bulk liquid fills this area, reforming this superheated layer and a new bubble will grow in its place. This is where the curve reaches the nucleate boiling regime and isolated bubbles are consistently generated in multiple locations on the surface. Eventually, the bubble frequency increases, the number of nucleation sites multiply and the isolated bubbles begin to interact with each other, forming slugs or columns of vapor. As more vapor is produced, the more difficult it is for saturated liquid to wet the surface, causing a decrease in slope of the curve. This peak or maximum heat flux is known as the critical heat flux(CHF). This is also known as the burnout point or boiling crisis as the sudden jump in surface temperature can approach material melting points and therefore damage systems. Next, is transition boiling, where bubble formation rapidly increases, causing vapor blankets to cover the surface. As vapor has a much lower thermal conductivity than liquid, the HTC and heat flux decreases as excess temperature continues to increase. Finally, the film boiling regime occurs at the Leidenfrost point or the point of minimum heat flux. At this point, the surface becomes completely covered by a vapor blanket. Therefore, heat transfers to the vapor completely through conduction or radiation, causing the heat flux to increase, sometimes even above the CHF of the nucleate boiling regime [4].

1.2.3 Performance Modeling

Pool boiling performance can be measured in terms of the heat transfer coefficient(HTC) or the ratio of the surface heat flux to the superheat temperature that is illustrated by the pool boiling curve, and the critical heat flux(CHF) or the maximum heat flux that is reached when heat transfer efficiency begins to deteriorate. These characteristics are affected by many conditions: gravity, pressure, heat flux, wall superheat, working fluid properties, surface characteristics and surface orientation, to name a few. Thus, to better understand the transport properties involved

in nucleate pool boiling, researchers have aimed to develop comprehensive, physics-based models for the HTC and CHF.

Two classical correlations for pool boiling heat transfer rate on plain copper surfaces are Rohsenow's correlation and Pioro's correlation [6]. They employ empirical constants including a proportionality constant and an exponent on the Prandtl number.

First, Rosenhow's correlation, with said constants C_{sf} and n of 0.0152 and 1.0, is given as [6]:

$$\frac{c_{p,f}\Delta T}{h_{fg}} = C_{sf} \left[\frac{q''}{\mu_f h_{fg}} \sqrt{\frac{\sigma}{g(\rho_f - \rho_g)}} \right]^{.33} \left(\frac{c_{p,f}\mu_f}{k_f} \right)^n \quad (2)$$

Second is the Piorro correlation, with a C_{sf} and m of .0152 and -1.1, given as [6]:

$$\frac{q''}{\Delta T_{sat} k_f} \sqrt{\frac{\sigma}{g(\rho_f - \rho_g)}} = C_{sf+} \left\{ \frac{q''}{h_{fg} \rho_f^{1/2} [\sigma g(\rho_f - \rho_g)]^{1/4}} \right\}^{2/3} \left(\frac{c_{p,f}\mu_f}{k_f} \right)^m \quad (3)$$

Two CHF prediction models for plain copper surfaces are the Zuber correlation and Liang and Mudawar correlation. In 1959, Zuber developed a hydrodynamic prediction of CHF based on both the Taylor wavelength and Helmholtz-instability, considering heat of vaporization, vapor and liquid densities and surface tension [7]. Zuber's model is given as:

$$q''_{CHF} = \frac{\pi}{24} \rho_g h_{fg} \left[\frac{\sigma g(\rho_f - \rho_g)}{\rho_g^2} \right]^{1/4} \quad (4)$$

Using deionized water at atmospheric pressure, the CHF is calculated to be $110W/cm^2$ [6].

Liang and Mudawar's model considers the heated surface orientation, producing the equation[6]:

$$q''_{CHF} = 0.151 \rho_g h_{fg} \left[\frac{\sigma g(\rho_f - \rho_g)}{\rho_g^2} \right]^{1/4} [1 - 0.0012\theta \tan(0.414\theta) - .122 \sin(0.318\theta)] \quad (5)$$

θ represents the heated surface inclination angle, with zero degrees being the surface is horizontal, upward facing. This model gives a CHF of $127W/cm^2$ [6].

1.3 Literature Review on Pool Boiling Performance

Although two-phase cooling has significantly improved thermal management systems, there are many parameters within pool boiling that can be modified to further enhance their heat transfer performance. Studies have investigated these modifications, finding strong correlations to (a) lower surface temperatures at the onset of nucleate boiling (ONB) (b) reduced and/or eliminated incipient temperature excursion c) reduced wall superheat throughout the nucleate boiling region (i.e., increasing the HTC) and (d) increased CHF to accommodate higher surface heat fluxes [8]. In figure 3, the black curve exhibits typical pool boiling behavior while the other red and blue curves exhibit the aforementioned enhanced boiling heat transfer characteristics.

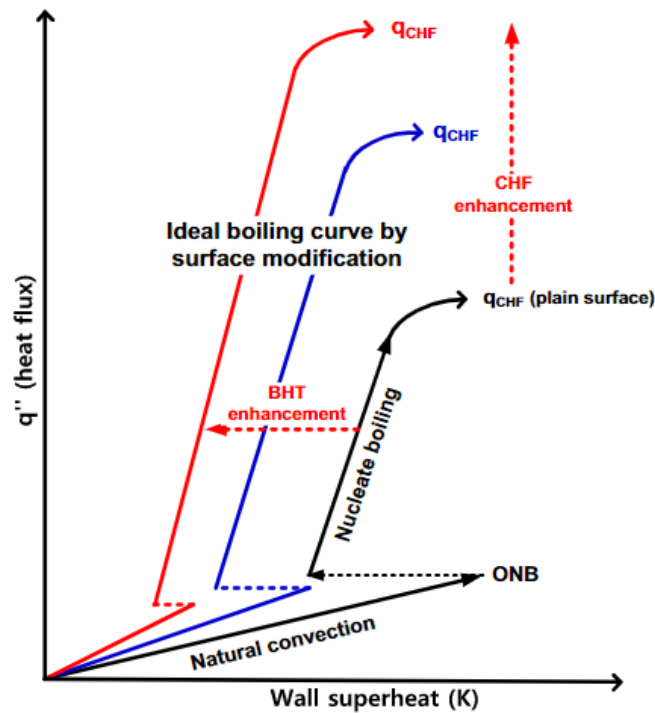


Figure 3: Ideal pool boiling curves [9]

According to Liang and Mudawar, application for pool boiling thermal management systems is relatively limited. The most important among these limits are CHF and maximum operating temperature brought on by material properties and reliability concerns. Figure 4 illustrates the constraints of temperature sensitive devices where the only acceptable scheme is that of the solid line where the boiling curve remains within the heat flux and temperature limits [10].

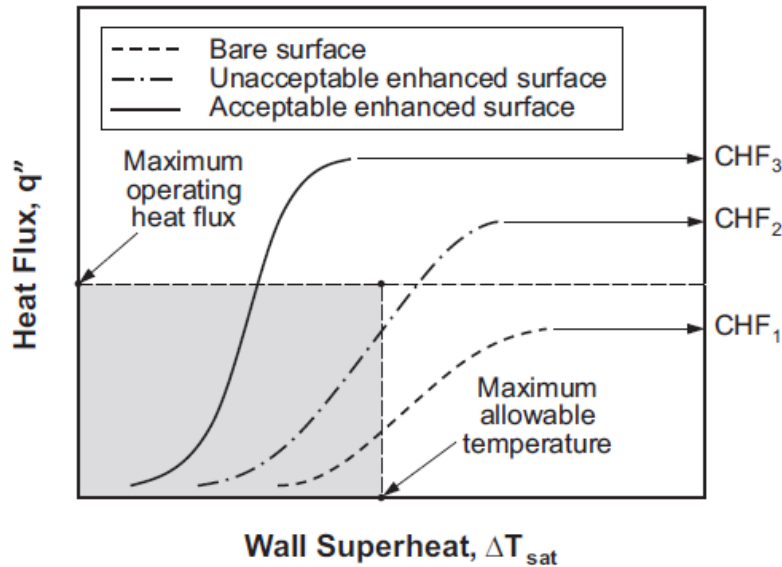


Figure 4: Optimum pool boiling curve for temperature sensitive devices [10]

As a result, researchers are continuously working to discover ways to overcome these boundaries with groundbreaking enhancement techniques, enlightening bubble statistic correlations, and innovative heat transfer prediction methods. However, although thermal engineers have the same end goal of improving heat transfer performance, due to the complexity of the boiling phenomenon and constraints of modern technology, there exist various agreeing as well as conflicting heat transfer findings that will be discussed in the sections to follow.

1.3.1 Heat Transfer Enhancement Techniques

As stated by Bergles et al. there are two methods of heat transfer augmentation; active and passive [11]. Active augmentation requires an external power to create mechanical mixing or rotation, surface and/or fluid vibration, electrostatic or magnetic fields and injection or suction. However, as these techniques complicate the boiling system and tend to impair reliability, passive techniques have become more widespread and have therefore been extensively researched over the last several decades [8]. Passive augmentation does not require an external power but rather relies on fluid and surface engineering such as suspending micro/nano particles in fluids or creating roughened or micro/nanostructured coated surfaces [8].

The major effective parameters regarding passive techniques to increase pool boiling performance involve surface and fluid properties. According to Chen et al. there are generally three main approaches to enhancing pool boiling heat transfer. The first being surface modification by increasing surface roughness, coating with microstructures or nanostructures or using nanoparticle suspension that result in particle deposition on the heater surface [12]. These methods have been found to increase the number of cavities that serve as nucleation sites as well as surface wettability through reduced contact angles. The second is to increase effective heat transfer surface area by introducing the thermal fin effect through microfabricated pin-fin structures. Finally, the third means of surface modification is employing wicking structures that delay dry out with the capillary pumping effect.

The first enhancement approach has been widely studied throughout literature. For example, a comparative analysis study by Hossain et al. investigated the effect of roughness and wettability of copper and brass surfaces on pool boiling performance. With an increase in the average surface roughness, heat transfer coefficient increased by 7% [13]. A study by Rioux et al. concluded that various scales of surface modifications can drastically improve boiling heat

transfer performance through different potential mechanisms. For instance, macroscale structures confront hydrodynamic issues in CHF by separating vapor columns, microscale structures provide capillary pumping effects for liquid replenishment to active nucleation sites through porosity and nanoscale structures enhance wettability through reduced contact angles. In addition, they proved further enhancement of heat transfer performance with the combination of the three scales of surface modifications [14]. Thiagarajan et al. compared thermally conductive, microporous, copper coated surfaces with varying thicknesses, porosity and cavity sizes to plain copper surfaces finding a 50%-270% increase in HTC as well as a 33%-60% enhancement of CHF [15]. Moreover, You et al. conducted pool boiling experiments with water-based nanofluids containing Al_2O_3 nanoparticles that produced a 200% increase in CHF in comparison to pure water [16]. Although nanofluids have been shown by almost all studies to enhance CHF, there are disagreeing results regarding its effect on HTC. A review on boiling heat transfer enhancement with nanofluids by Barber et al. provides a detailed scope into the conflicting data presented in past literature [17]. She concludes that further systematic experiments must be performed to comprehend this contradicting data.

Moving onto the second approach, Kong et al. tested bistructural surfaces based on micro-pin-fins, discovering an increased vitality of bubbles that grow, collide, merge and move rapidly from the microfins to nearby smooth channels [18]. Their experimental results reveal a CHF enhancement of over 120% compared to a smooth surface, indicating the favorable impact of micro-pin-fin structures on heat transfer performance [18].

For the third approach, pool boiling experiments were carried out by Chen and Li to study the combined effect of wicking and modulated wavelength on CHF. They fabricated two-tier surfaces by creating copper nanowires with electrodeposition on wire-cut microgrooved

surfaces. CHF was found to increase 119.3% in comparison to plain copper surfaces due to liquid replenishment via microgrooves, hydrodynamic instability from the modulated wavelength and liquid wicking in the copper nanowires that delay spreading of dry-out spots [19].

1.3.2 Bubble Dynamics

Now that we have an idea of various existing enhancement techniques, it is essential to also grasp how they impact heat transfer performance. The primary way is through bubble dynamics. It has been widely accepted that the high heat transfer rates encountered in nucleate boiling are mainly due to the motion of bubbles in the superheated liquid adjacent to the heater surface [20]. As a result, many have investigated the ability to control bubble behavior with surface and fluid modifications in order to optimize heat transfer. Although these bubble dynamics have been greatly studied, there are still inconsistencies in their predictions and correlations to boiling performance as the extraction of nucleation statistics has proven intrusive and highly variable. This section will thus explore the crucial bubble dynamic parameters previously considered in theoretical models: active nucleation site density, bubble departure diameter, and bubble departure frequency.

Active nucleation site density is the number of fixed sites or cavities where bubbles form in a given area of a surface heater. Information on this parameter is essential to determining the amount of evaporative energy carried away as bubbles lift off the boiling surface and thus predicting heat transfer performance. Recognizing this significance, researchers have developed correlations in an attempt to predict active nucleation site density. Many of which report its dependence on the following; heat flux, wall superheat, contact angle, cavity size and cavity geometry [21][22][23][24][25].

Overall, an increased number of nucleation sites has been assumed to provide increased bubble activity resulting in more convection heat transfer and/or increased latent heat transport. Therefore, in the process of optimizing surfaces, many enhancement techniques, discussed in the previous section, are aimed to increase the number of active nucleation sites. For instance, a study by Mori and Utaka reviewed the enhancement of CHF through surface modification and found that CHF can be improved by increasing the number of nucleation sites [26]. Abd elhady compared boiling curves of pure water using clean and nanoparticle deposited surfaces and found that heat transfer rate increased with the increase in roughness from 20 nm to 420 nm due to the higher number of active nucleation sites [27]. However, when using Al_2O_3 nanofluids on these same surfaces, heat transfer rate decreased with an increase in surface roughness. It was believed that nucleation sites deactivated as the alumina nanoparticles in the fluid deposited on the surface [27]. Additionally, Thiagarajan and colleagues' pool boiling experiments on microporous coated copper surfaces showed enhanced nucleate boiling heat transfer as a direct result of its significantly higher active nucleation site density [15]. In contrast, Ranjan et al. fabricated nanoneedle surfaces, with increased wettability and wickability properties in comparison to plain surfaces. These anodized surfaces ultimately showed a higher CHF however, they had fewer active nucleation sites [28]. Hence, due to the many variables involved in pool boiling experiments as well as the difficulty of measuring active nucleation site density with such chaotic bubble motion, studies show conflicting results.

Bubble departure diameter is defined as the equivalent diameter of the vapor bubble once it entirely departs from the nucleation site. There are different approaches to predicting this parameter including force balance analysis which analyzes the mechanism of the departure process and empirical correlations that rely on experimental data [29]. According to Zeng et al., bubble departure occurs when the balance between buoyancy, surface tension, contact

pressure, shear lift and bubble growth force is violated. Using the force balance approach, they derived the equation [30]:

$$D_d = 2 \left[\frac{3k^{2/n}}{4g} (10n^2 + n(n-1)) \right]^{2/(2-n)} \quad (6)$$

Applying averaged experimental, departure data, Cole modeled bubble departure diameter as a function of the Jakob number, or the ratio of sensible to latent heat absorbed during phase change processes, obtaining [31]:

$$D_d = 0.04 J a \sqrt{\sigma/g(\rho_l - \rho_v)} \quad (7)$$

Bubble departure diameter can thus depend on these net forces as well as unique experimental conditions such as wall superheat, heat flux, pressure, contact angle and thermophysical properties of the working fluid. However, there is no general prediction model for it as there is a large discrepancy in influential parameter correlations among existing models, as depicted in figure 5. MahMoud believes that this scatter in results is due to the differences in experimental boundary conditions, surface structure and material, uncertainty in diameter measurements due to deformed shaped bubbles, and definition of equivalent bubble diameters [32].

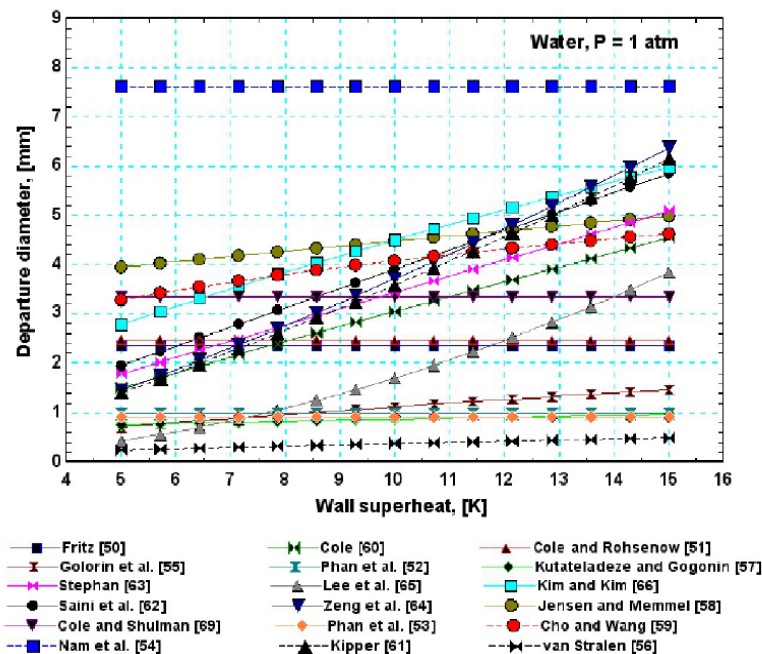


Figure 5: Comparison of bubble departure diameter prediction models [32]

Improved heat transfer rates have been linked to bubble departure diameter under these varying conditions. For example, Može et al. investigated the boiling of self rewetting fluids on untreated surfaces, revealing an increased CHF with decreased bubble departure diameters from lower surface tension [33]. The smaller bubble departure diameter generally results in a quicker bubble cycle, allowing more heat to dissipate as more bubbles release from the surface. On the contrary, a comparative study by Hossain et al. revealed that boiling on microgrooved surfaces produced better heat transfer performance and larger bubble departure diameters than on a flat surface. It is assumed that the rougher the surface, the larger the cavities where the bubble forms. With more surface area of each cavity, the greater the surface tension force which holds the bubble down, allowing the bubble to grow larger before departing. Therefore, their results show improved HTC with larger departure diameters [13].

Bubble departure frequency is the number of bubble cycles per unit time at a given nucleation site. It can be found by taking the reciprocal of the summation of the bubble waiting time; the period from the moment the previous bubble departs to the point the current bubble nucleates, and the bubble growth time; the period from when the bubble nucleates to the moment it departs [34]. Bubble departure frequency is intimately related to bubble departure diameter and therefore also has many disparities within prediction models. Bubble departure frequency can typically be written in the form of $fD_d^m = f(\rho_l, \rho_v, g, \sigma, \alpha_l, Ja)$. The left hand side, where m is an empirical value, is fitted as a function of liquid and vapor density, gravity, surface tension, thermal diffusivity, and Jacob number [35].

Applying relations and observations from previous studies for boiling on a horizontal surface, in 1959, Zuber deduced this trend [7]:

$$fD_d = 0.59 \left[\frac{\sigma g(\rho_l - \rho_v)}{\rho_l^2} \right]^{1/4} \quad (8)$$

In 1960, Cole equated the rate at which the bubble rises, the buoyancy force and the drag force on a free rising vapor bubble, deriving [36]:

$$fD_d^{1/2} = \left[\frac{4g(\rho_l - \rho_v)}{3C_d \rho_l} \right]^{1/2} \quad (9)$$

where C_d is the drag coefficient. In 1966, Ivey presented three correlations for different regions as follows [37]:

For the hydrodynamic region:

$$fD_d^{1/2} = 0.9g^{1/2} \quad (10)$$

For the transition region:

$$fD_d^{3/4} = 0.44g^{1/4} \quad (11)$$

For the thermodynamic region:

$$fD_d^2 = \text{constant} \quad (12)$$

More recently, Zhang et al. proposed a unified relationship between bubble departure frequency and diameter for various combinations of heating substrates and working fluids in saturated nucleate pool boiling. Their relationship takes the following form [38]:

$$f^* D^* = 1 \quad (13)$$

where $f^* = \frac{f}{4.5^2 \left(\frac{k_l}{k_s}\right)^2 (v_l \alpha_l)^{-1/2} \alpha_s g^{1/2}}$ and $D^* = D^{1/2}$

As seen, even after extensive research for over half a century, there is no generalized correlation for bubble departure frequency.

Researchers have also attempted controlling bubble departure frequency in order to improve boiling performance. According to Kim, the consistent contributing factor to nucleate boiling enhancement using microporous coatings is the increase in bubble departure frequency [39]. A rise in bubble departure frequency means reduced waiting and/or growth time, simultaneously inhibiting the growth of the superheated liquid layer and enabling the removal of larger amounts of superheated liquid. This leads to a lower surface temperature and consequently reduced wall superheat. Further, in a paper by Dong et al., pool boiling experiments are carried out with ethanol to study the effects of micro/nanostructures on bubble nucleation, bubble departure and nucleate boiling HTC. It was found that nanostructures increased departure frequency due to their capillary wicking effect. This delayed bubble merging, preventing vapor film formation and thus reduced wall superheat and enhanced CHF [40]. Bertossi et al. performed experiments using carbon nanotube coated surfaces to highlight their influence on nucleation mechanisms. They attributed their heat transfer intensification to a higher frequency of bubble emissions along with an enhanced number of nucleation sites [41].

Researchers have also developed pool boiling mechanistic models for heat flux that heavily rely on these bubble dynamics (i.e., active nucleation site density (N_b), bubble departure diameter (D_b) and bubble departure frequency (f_b)). According to the heat flux partitioning model, first proposed by Kurul and Podowski, the total boiling heat transfer rate can be obtained by summing the different heat transfer modes of natural convection, quenching, and evaporation [42]:

$$q''_{tot} A_{tot} = q''_{nc} A_{nc} + q''_q A_q + q''_{ev} A_{ev} \quad (14)$$

This equation can then be manipulated for heat flux:

$$q''_{tot} = q''_{nc} A_{f,nc} + q''_q A_{f,q} + q''_{ev} A_{f,ev} \quad (15)$$

Where A_f is the area fraction of those specific regions. The area available for heat transfer can also be divided into the area of influence of bubbles where q''_{ev} and q''_q take place and the non-active area where q''_{nc} occurs [43].

Different correlations and conditions have been applied, resulting in various equations for these heat transfer modes. In Kurul and Podowski's model, these heat flux modes can be defined as [42]:

$$q''_{nc} A_{f,nc} = \left[0.14 \frac{k_f}{L_c} Ra^{1/3} \Delta T \right] \left[1 - \pi R_b^2 N_b \right] \quad (16)$$

$$q''_q A_{f,q} = \left[\frac{2k_f}{\sqrt{\pi \alpha_f t_w}} \Delta T \right] \left[3\pi R_b^2 N_b \right] \quad (17)$$

$$q''_{ev} A_{f,ev} = \left[\frac{4}{3} R_b \rho_g h_{fg} f_b \right] \left[\pi R_b^2 N_b \right] \quad (18)$$

Where R_b is the bubble departure radius that is equivalent to $\frac{1}{2}D_b$ and ΔT is the wall superheat. In equation 16, k_f is the thermal conductivity of the liquid, L_c is the heater size and Ra is Rayleigh's number. Then in equation 17, t_w is the bubble waiting time, ρ_g is the vapor density, and h_{fg} is the latent heat of vaporization.

A study by Kim and Kim incorporated the impact of bubble coalescence from high heat fluxes, modifying Kurul and Podowski's partitions. While they found that coalescence does not significantly affect the heat fluxes, they found that it affects the area fractions [44]. Benjamin and Balakrishnan present a similar model where they assume an area of influence is four times the projected area of the bubble at departure, deriving heat flux expressions of [43];

$$q''_{nc} = h\Delta T \left[1 - N_b \pi D_b^2 \right] \quad (19)$$

$$q''_q = 2\Delta T \sqrt{\frac{k_l \rho_l C_{pl}}{\pi t_w}} \left[N_b \pi D_b^2 \right] \quad (20)$$

$$q''_{ev} = V_{ev} \sqrt{t_g} \rho_l \lambda N_b \quad (21)$$

Where in equation 19, h is the estimated heat transfer coefficient, in equation 20, C_{pl} is the specific heat of the liquid, and in equation 21, V_{ev} is the volume of liquid evaporated during bubble growth time.

Overall, past studies have made it evident that bubble dynamics such as active nucleation site density, bubble departure diameter, and bubble departure frequency can be strong regulators as well as gauges of boiling heat transfer performance. However, there are still dubious and inconsistent correlations between these boiling features that must be further explored.

1.3.3 Heat Transfer Prediction Methods

Quantification of heat transfer performance has been heavily studied using theoretical, numerical and experimental techniques [45]. However, as seen from previous literature, the many parameters involved in pool boiling make it difficult to accurately predict heat transfer using these classical correlation techniques. For example, Kandlikar developed a theoretical model to predict CHF, incorporating the impact of contact angle and surface orientation through force balance analysis. He tested his model with available data sets from literature for different fluids, correctly estimating CHF for superhydrophobic surfaces however underestimating for hydrophilic ones [46]. Based on experimental data, Du et al. found that bubble growth rate and bubble departure diameter in nucleate pool boiling are strongly influenced by system pressure and Jakob number. With this, they created a modified theoretical model for predicting these bubble dynamics. Although finding better agreement with experimental data compared to several previous models their prediction error was $\pm 50\%$ [29]. Dhir proposed a complete

numerical simulation of bubble dynamics and associated heat transfer processes to predict the boiling curve. Although his numerical simulation predictions seem to be in agreement with experimental results, it is stressed that only low heat fluxes were numerically analyzed [47]. As a result, numerous empirical correlations and mechanistic models have been proposed regarding pool boiling; many of which are derived by applying theory of similarity and related dimensionless numbers, where their powers and proposed constants are determined by matching the modeling results with experimentally measured data [48]. Additional correlation examples are those of Rohsenow and Piro which can be found in section 1.2.3. However, as described, the broad range of parameters in pool boiling have made it challenging to create a model that spans all possible conditions, resulting in simplified predictions that become suspect when applied to new situations. Thus, the accuracy of heat transfer correlations is limited to specific boiling conditions or assumptions applied in their development [48].

The questionable reliability of theoretical and numerical models has made it difficult to draw broader conclusions on dynamic boiling physics, compelling researchers to depend on experiments to measure heat transfer performance. However, up until around 1980, previous experimental methods were leaving out a crucial aspect; visual data. Nakayama et al. carried out one of the first visualization studies, correlating vaporization and enhanced heat transfer by analyzing bubble formation characteristics with boiling images [49]. Their solutions gave the predictions of population density of active sites and frequency of bubble formation which were then used to predict convective heat flux [50]. Since the discovery that boiling images are richly embedded with quantitative measurements of the dynamic boiling phenomenon, high-speed visualization of pool boiling experiments has enabled the analysis of boiling performance enhancement techniques and development of pool boiling curves based on bubble morphologies [45][51][52][53][54]. But, as more researchers recognized the efficacy of boiling images in regards to understanding boiling physics; the more apparent the obstacle of

post-processing became. In order to extract bubble parameters, images had to be manually measured frame by frame, taking hours to days to accomplish [54]. Robert Patsuzko visually investigated boiling heat transfer for extended surfaces called narrow tunnel structures, determining heat fluxes based on observed bubble parameters. His method was to define bubble departure diameter as an arithmetic average of the maximum and minimum diameters that were manually computed by pixel counts for five superheats [54]. It was also pointed out that when determining departure frequency by counting the number of escaping bubbles on 100 recorded frames, additional bubbles could have been added or omitted by mistake [54]. Evidently, despite the significance of gathering essential visual information, current measurement setups fail to analyze image data without extensive user involvement, which is not only time-consuming but also introduces error through user bias [45]. To address this problem, major efforts have gone into developing image based machine learning(ML) algorithms, known as computer vision, that can bridge this gap between measurement and visual information.

1.4 Thesis Objectives

There exists an abundance of literature and data on endless combinations of pool boiling conditions, revealing ideal boiling characteristics for enhanced heat transfer performance along with various correlations and prediction models. However, conventional measurement and analysis techniques introduce error through various assumptions and biases(e.g., experimental or user) On the other hand, the tedious and often intrusive steps to achieve such results are rarely acknowledged. This task becomes even more cumbersome when visual data is involved, requiring extensive user involvement for bubble analysis. A great deal of time has gone into post processing in order to obtain results that seldom provide clear and detailed descriptions of boiling physics. Thus, the objective of this thesis is to present a non-invasive, automated computer vision model capable of accurately and efficiently quantifying pool boiling bubble dynamics to predict heat transfer performance. This study seeks to not only contribute a means

to detailed data on active nucleation site density, bubble departure diameter and bubble departure frequency but also to improving correlations of these parameters to the pool boiling process. Future work will focus on exploiting such relations to enhance boiling heat transfer performance and shed light on underlying mechanisms that govern this phenomenon. To further aid in the accuracy of results obtained from thermal and visual data, an optimized pool boiling setup was developed for experimental procedures. Ameliorated methods of acquiring necessary data are also explicated to assure optimal performance of our vision-based approach to analyzing pool boiling characteristics.

CHAPTER 2: COMPUTER VISION MODEL

This chapter will delve into the previous efforts of integrating machine learning techniques into visualization studies to facilitate learning pool boiling physics. It will then introduce our own computer vision model, thoroughly explaining its framework, training, feature extraction and validation process.

2.1 Introduction to Computer Vision

An area of machine learning (ML) dedicated to interpreting and understanding visual imagery is known as computer vision. With provided concrete data points, information can be extracted from inputted images or videos to understand or predict results similar to and sometimes even better than how the human brain does. Some familiar ML-based computer vision applications are automated self-driving, facial recognition, and disease diagnosing [55]. More recently, computer vision has found its way into the thermal science field, enabling researchers to learn physical laws from highly dimensional noisy data such as boiling images [56].

With available pool boiling data, ML-based computer vision models have been trained to predict boiling regimes, bubble statistics, heat flux and heat transfer coefficients from experimental images. For example, in order to accelerate the analysis of infrared thermometry studies of boiling heat transfer, Ravichandran and Bucci presented a machine learning algorithm to be used in quasi-real-time or as fast as they can practically run an experiment. This algorithm uses a feed-forward artificial neural network (FFNN) to measure bubble growth time, bubble period, and nucleation site density directly from infrared radiation videos with a regression coefficient of .95 and higher when compared to conventional image processing techniques [57]. Hobold and da Silva demonstrate boiling regime classification for an on-wire pool boiling setup using simple machine learning and image processing techniques. Trained on low-speed and low-resolution

data, their support vector machines(SVM's) and multilayer perceptron neural networks(MLPNN's) were able to identify boiling regimes with an accuracy up to 99% [55]. With the same setup, Hobold and da Silva also showed correlations between bubble morphologies and heat flux using MLPNN's, obtaining a mean absolute percentage error of 9.84% [56].

A more complex and efficient machine learning algorithm is the convolutional neural network(CNN). CNN's have become a dominant method in computer vision tasks as they are designed to simulate the deep and hierarchical structure of neural networks structures in the human brain by systematically learning from multiple features through multiple operation layers [58]. They accept the pure image pixels and find themselves the features that best classify the data, thus requiring less preprocessing compared to other image-based methods. In addition, CNN enhances its own performance as each layer transforms the data from one state to another [59]. This ability makes CNN highly attractive in the machine learning subfield called deep learning(DL), where features do not need to be defined. Applications of CNN-based computer vision are hence rapidly progressing in the thermal science field to better understand boiling heat transfer. The approach to estimate different local boiling characteristics such as bubble growth rate, departure diameter, departure frequencies, nucleation site density, evolution of bubbles and dry spots, through visual analysis and CNNs is demonstrated in a study by Chernyavskiy and Malakhov. They employ a CNN based instance segmentation model(Mask R-CNN) that successfully detected bubbles from images captured from the bottom size of a transparent pool boiling heated surface [60]. A study by Chatterjee demonstrated this capability of deep learning CNNs by automatically segmenting dry areas from IR images captured during pool boiling heat transfer. This CNN framework was then evaluated by measuring the accuracy of dry area fraction, bubble frequency and bubble density quantification. According to their results their model proved satisfactory, predicting these parameters for increasing heat flux with consistency. However, their observed bubble dynamics did not follow theoretical behavior [61].

In a separate on-wire pool boiling study by Hobold and da Silva, they again classified boiling regimes but now using a trained CNN. From solely departed bubble dynamics and bubble morphology, they received an accuracy of over 99%. They then applied Bayes' theorem to their algorithm, looking at several sequential frames to detect the transition from nucleate boiling to film boiling [62]. Furthermore, they predicted heat flux using CNNs with less than 10% error [57]. Rassourlinejad-Mousavi et al. employ an image-based deep learning model trained on extracted images from pool boiling youtube videos for identification of three boiling regimes; discrete bubbles, bubble interference and coalescence and CHF. In addition to CNNs, they study transfer learning(TL) models that pretrains a DL model using a larger data set and then use the small dataset from the target domain to fine-tune parameters. Their TL model outperformed CNN, retaining a high accuracy ranging from 90.02% to 98.71% whereas their CNN models obtained an accuracy ranging from 68.20% to 98.24% [63]. These deep learning approaches have therefore proven their potential in enabling automated image analysis for classifying heat transfer performance and boiling regimes; however, this image evaluation gets very complicated when dealing with bubbly flows. As a result, to improve algorithm reliability, Hessenkemper et al. employ multiple CNN's to tackle the tasks of segmentation and reconstruction for better identification of individual bubbles despite overlap and occlusion. With pixel-to-pixel prediction CNN's, they achieved satisfactory results in accurately determining bubble size and gas volume fractions [64].

Overall, researchers have begun to exploit visual information to gain knowledge on boiling physics, even employing machine learning algorithms to further enhance experimental accuracy and efficiency. However, much of the literature discussed either classifies heat transfer performance, boiling regimes, or bubble dynamics but does not further link these boiling features together. Moreover, the extracted visual data is limited to on-wire pool boiling which cannot represent the erratic bubble behavior produced on 2-D or 3-D surfaces. Accordingly,

there are very few works relating realistic bubble dynamics of active nucleation site density, bubble departure diameter, and bubble departure frequency to quantifiable thermo-hydraulic parameters(i.e., heat flux and heat transfer coefficients) using computer vision techniques.

Although decades of studies have unveiled the potential to understand underlying boiling mechanisms through bubble analysis, the relation between these parameters and boiling processes are still unclear and inconsistent. This is partially due to the natural emission of hundreds of bubbles per second, that all individually exhibit complex movements, interactions and morphologies [65]. This further complicates the extraction of such boiling bubble dynamics, where individual features must be connected throughout time [65]. With the objective to address these challenges and fill this gap in knowledge, we employ a data driven framework that autonomously captures spatio-temporal bubble statistics and quantifies heat transfer performance from high-quality boiling images.

2.2 Model Framework

To predict real-time boiling heat transfer characteristics from bubble behavior, we employ our computer vision based framework that is composed of three main components; an object detection module, an object tracking module and a data processing module [65].

First, the object detection module employs the deep learning instance segmentation model, called Mask R-CNN that automatically detects and generates pixel-wise masks for every object(i.e., bubbles) in an image. Each bubble mask is then assigned a unique identifier to record spatial features such as equivalent diameter, pixel-wise area, eccentricity, orientation, solidity, and location. These masks are then processed through the object tracking module(TrackPy) where a k-dimensional(k-d) tree algorithm uses the identified spatial features as parameters for linking masks with respect to time. During bubble tracking, potential errors in

trajectories are manually identified and corrected using a documented graphical user interface(GUI). Lastly, the tracked spatio-temporal features are post-processed through a commercial programming software(MATLAB) to extract higher-level features such as active nucleation site density, bubble departure diameter, bubble departure frequency and heat flux.

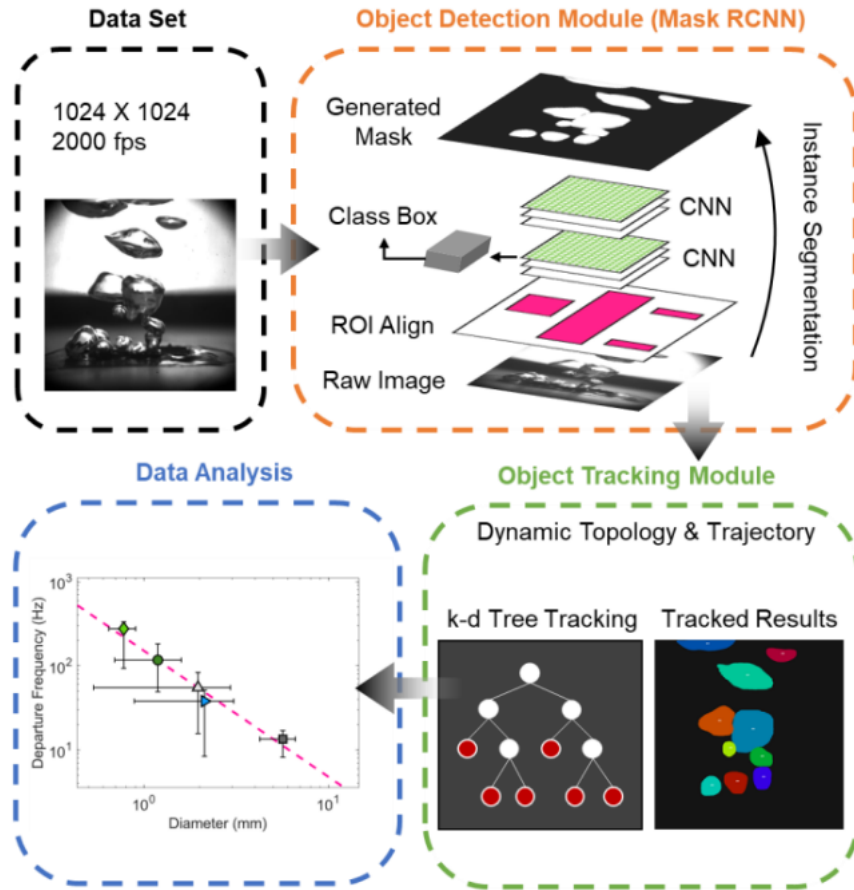


Figure 6: Computer vision model framework flowchart including the object detection module, object tracking module, data processed module [65]

2.3 Mask R-CNN Training

For automated image analysis, we first had to train our Mask R-CNN, instance segmentation model. In order to learn features of an object, Mask R-CNN needs labeled data in the form of pixel-wise image annotations. Thus, images were manually annotated using an online commercial software(Supervisely, San Jose, USA). Extracted pool boiling images were

uploaded to Supervisely where weeks went into carefully tracing and labeling thousands of bubbles in the region of interest. An example annotated image is illustrated in figure 7b. To better guarantee accurate bubble detection, it was imperative to properly trace each bubble, even those overlapping, merging, or even partially in shot. Then to mitigate user bias, images were randomly selected and augmented to diversify the dataset, improving generalizability of the model and therefore its robustness [66]. The total augmented training data set was split where 80% of these images went to training and 20% went to testing. Training datasets are labeled with calculated heat fluxes from experimental measurements while test datasets are unlabeled to verify the model's ability to accurately analyze new images. The initial model uses weights pre-trained on the Microsoft Common Objects in Context(MSCOCO) dataset [67]; however they are adjusted throughout training to increase detection accuracy. The model trains for 100 epochs using stochastic gradient descent with a learning rate of $1e-3$ and momentum of 0.9, saving the model's state after each epoch. The optimal model, or epoch with the lowest test loss was selected [45].

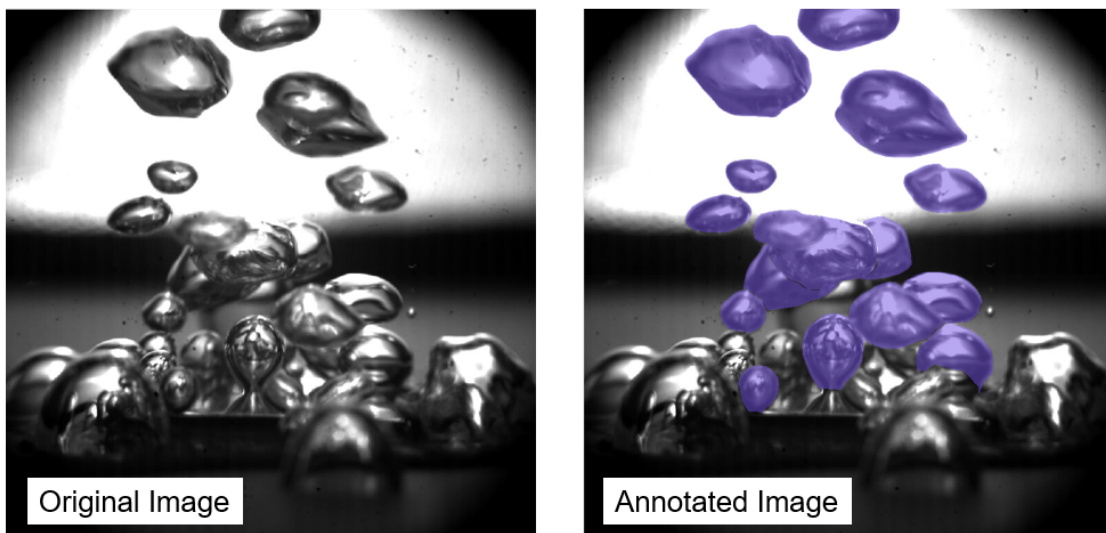


Figure 7: Supervisely annotation of pool boiling image (a) original image (b) annotated image

2.4 Feature Extraction

For characterizing higher-level features such as the active nucleation site density, bubble departure diameter, and bubble departure frequency from our spatio-temporal features, we used a custom algorithm. Bubble departure events are detected by comparing the bottom bounding box's relative position to the surface with the logic of; $IF(bbox_{bot,1} < y) AND iF(bbox_{bot,2} > y)$, where $bbox_{bot,t}$ is the bottom bounding box coordinate at time t and y is the pixel value corresponding to the boiling surface location [65]. The nucleation site density is estimated as;

$$N_b = \left(\frac{1}{Z} \sum_{j=1}^Z x_j\right) / A_s \quad (22)$$

where j is the time, x_j is the number of bubbles on the surface at that time, Z is the total number of time steps, and A_s is the projected boiling surface. The departure diameter(D_b) is the equivalent diameter predicted from our model of bubbles within the bottom bounding box. Then, as the bubbles were observed to form immediately after departing, we equated bubble waiting time to zero, obtaining the departure frequency as;

$$f_b = \frac{1}{t_g} \quad (23)$$

where t_g is the bubble growth time(i.e., time between nucleation and departure).

2.5 Model Validation

The model's object detection and tracking modules were validated by testing accuracy, recall, precision, F1-score, mean average pixel error(MAPE) and occlusion-induced error. A developed MATLAB script binarizes the data sets to compare pixels, checking if the predicted ones(i.e., predicted mask(PM)) corresponded to our annotated ones(i.e., ground truth(GT)). A true positive(TP) instance is when the model detects an instance that matches the GT whereas a false positive(FP) instance is when the model predicts a nonexistent object. True negative(TN)

is when the model correctly predicts no existing instances and a false negative(FN) is when an existing object is not detected. The performance metric equations of the object detection model are defined as [65][68][69]:

$$Accuracy = \frac{TP + TN}{TP + TN + FN + FP} \quad (24)$$

$$Recall = \frac{TP}{TP + FN} \quad (25)$$

$$Precision = \frac{TP}{TP + FP} \quad (26)$$

$$F1\ Score = 2 * \frac{\{Precision * Recall\}}{(Precision + Recall)} \quad (27)$$

$$MAPE = \frac{1}{n} \sum_{i=1}^n \left| \frac{GT-PM}{GT} \right| \times 100 \quad (28)$$

Figure 8 illustrates the exceptional performance of the computer vision model, with all metrics achieving values greater than 90%. Also, the model reported a MAPE of 1.56% [65].

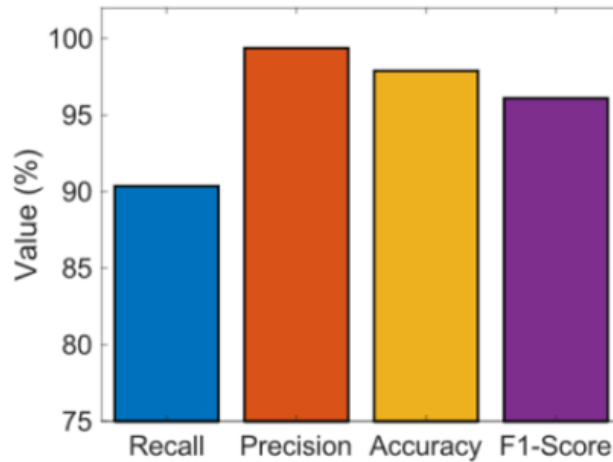


Figure 8: Model performance metrics for validation [65]

Occlusion-induced error is mainly caused when bubbles block each other resulting in improper bubble detection and therefore invalid spatio-temporal data. To determine occlusion-induced error, datasets with over 200 randomly labeled images at various heat flux steps were manually compared with model predictions. This performance metric was estimated on surface bubbles achieving a maximum occlusion-induced error of 4.6% [65].

CHAPTER 3: OPTIMIZED POOL BOILING SETUP

Within our lab, pool boiling experiments were previously carried out using an older setup. With continuous usage over the years by different researchers who ran various types of pool boiling procedures, the performance of this setup began to deteriorate. For instance, components had broken or become contaminated with chemicals. In addition, as tests were run, it became obvious that certain aspects to the setup design could be greatly improved. As pool boiling rigs are used to study such a chaotic phenomenon under varying complex conditions, there are many parameters that must be considered when running experiments. For example; thermal insulation, material strength, leakage, data acquisition, visualization for imaging, etc. Therefore, in order to accurately observe and measure heat transfer performance with our computer vision technique, it is crucial to ensure a robust and efficient pool boiling setup. Throughout this chapter, the steps to optimizing our pool boiling setup will be described in detail, beginning with the preliminary design all the way to it's final assembly. The experimental setup process can be divided into four categories; structural design, vendor search, subsystems design and final setup assembly.

3.1 Structural design

The main structure of our design consists of a liquid chamber, heating block, upper and lower insulation bases, and a lid. When designing these components, we prioritized structural integrity, thermal insulation and overall experimental efficiency.

The material of our rectangular tubed liquid chamber was changed from polycarbonate to glass. In comparison to polycarbonate, glass is more clear, more resistant to scratches and has a higher melting point. Therefore, glass provides better visualization and reduces the chances of overheating and shattering, which occurred in our previous setup. However, as the strength of

glass is significantly lower than polycarbonate, the chamber must be handled with caution and carefully monitored during experiments. In addition, rectangular, laser-cut, rubber gaskets are placed on both ends, between the chamber and the base as well as the lid to prevent water and vapor leakage.

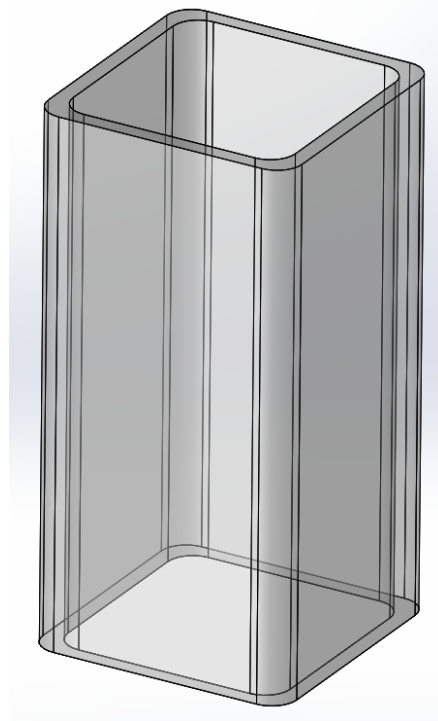


Figure 9: Liquid chamber design

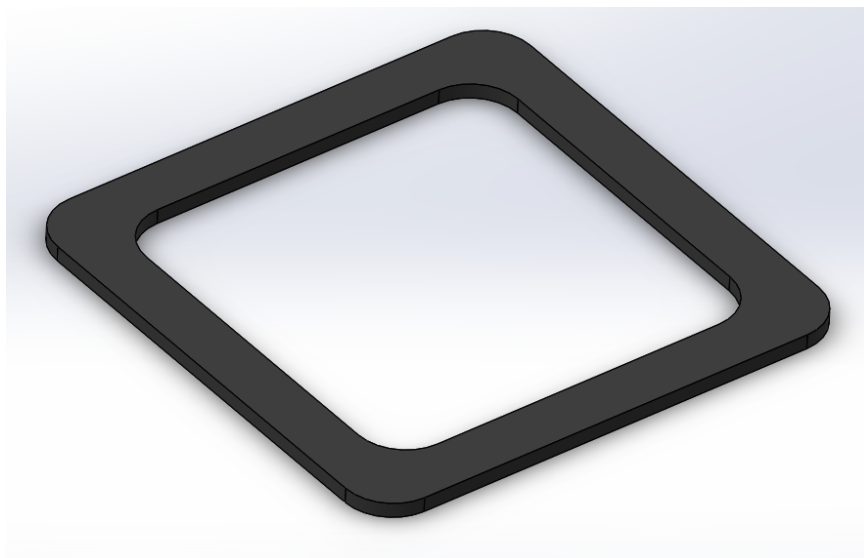


Figure 10: Rubber gasket design

The heating block is made of copper 101, as this grade offers a higher thermal conductivity due to its 99.9% purity. It consists of a cubical portion measured as 50.8mm x 50.8mm, where cartridge heaters are inserted from the bottom. From the top, a 10mm x 10mm square fin is extruded. The top of this fin serves as the heating surface where test samples will be directly mounted. In comparison to the old setup, this heated surface is now slightly elevated from the surrounding surface by .3mm(Figure 12), enabling improved sealing techniques with epoxy when mounting our samples. On one side of this fin, thermocouples are embedded by 5mm into precisely dimensioned and drilled holes. As the previous heating block had significant machining errors, the distance between thermocouple holes all varied from one another (i.e., 8.51mm, 8.24mm and 7.57mm), ultimately complicating calculations and introducing error. Thus, we ensured exact placement of our thermocouple holes that are 10mm apart from each other and 7mm away from the heated surface(Figure 13). We also reduced the volume of our copper block by approximately 3000 cubic millimeters. The length and width of the cubical portion was slightly decreased by 0.8mm and the fin height was shortened from 50.8mm to 38.4mm. The smaller the heating block, the quicker it will heat up to begin experiments as well as reach steady state for each step in heat flux. This will also allow for quicker cool down once CHF is reached and a more uniform temperature distribution for accurate temperature readings.

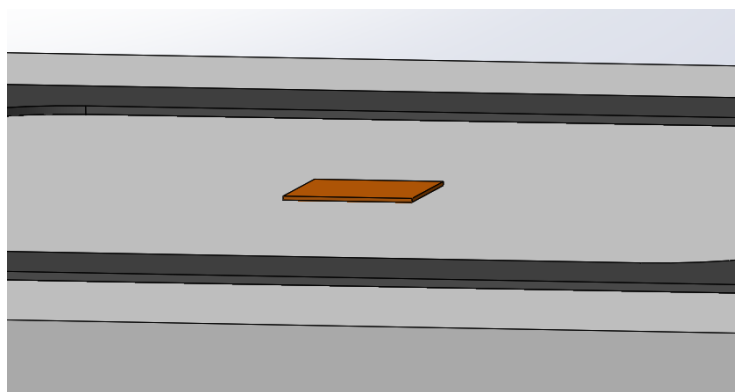


Figure 11: Elevated heated surface

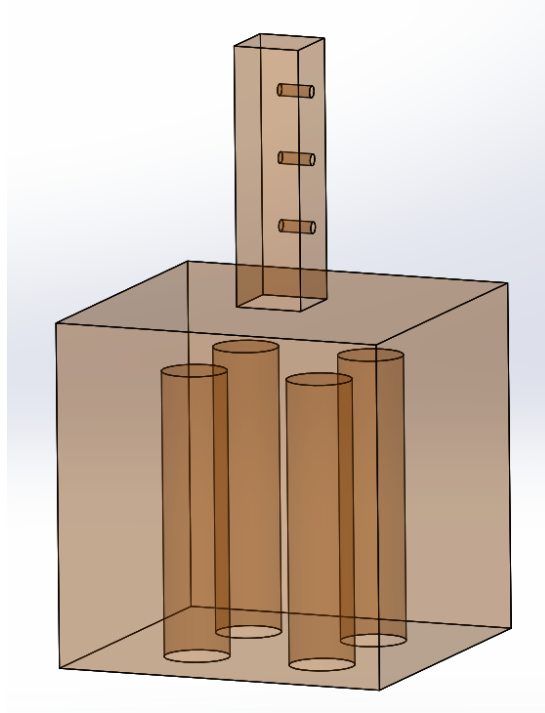


Figure 12: Heating block design

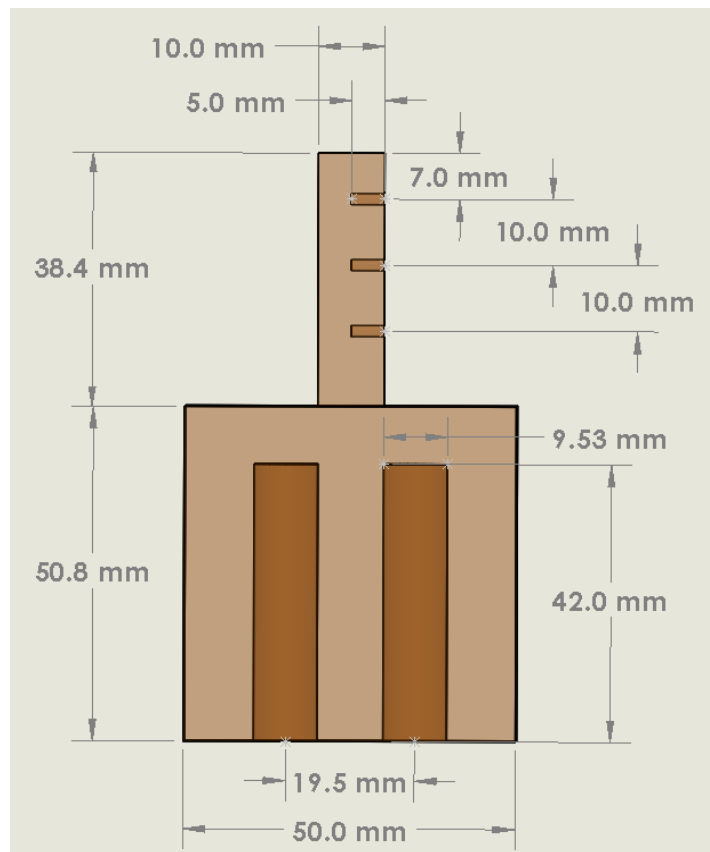


Figure 13: Heating block dimensions

The insulation bases that surround the fin of the heating block(upper base) and lie below, supporting the heating block(lower base), are made out of Poly Tetra Fluro Ethylene(PTFE) or commonly known as Teflon. After analyzing different thermally resistant materials, PTFE provided the lowest thermal conductivity and highest service temperature, ensuring minimal heat loss and damage to our system. In the upper base, three holes are precisely drilled for the thermocouples for a tight and accurately aligned fit into the copper fin, illustrated in figure 18. A shallow pocket is also machined into the top to perfectly fit one rubber gasket, creating an air-tight seal for the liquid chamber. The old design had a majority of the copper fin exposed to air due to a large pocket in the bottom of the base. To determine if this design was optimal for insulation, we carried out a thermal resistance and heat transfer analysis between teflon and air.

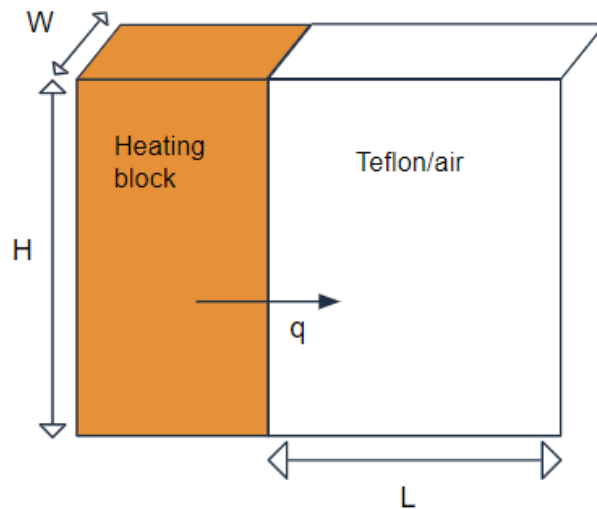


Figure 14: Schematic of heat transfer from heating block to air/teflon

The dimensions in the schematic are defined as; $L = 0.0412m$, $W = 0.01m$, $H = 0.05m$, giving a heat transfer surface area of; $A_s = H \times W = 0.0005m^2$

The thermal resistance of and heat transfer through conduction to teflon is calculated as follows:

$$k_{teflon} = .25W/mK$$

$$R_{teflon} = \frac{L}{k} = \frac{.0412m}{.25W/mK} = .1648 [m^2K/W] \quad (29)$$

$$q_{teflon} = k_{teflon} A_s \Delta T / L = .0005(\Delta T) / .1648 = 3.0340 \times 10^{-3} (\Delta T) [W] \quad (30)$$

Applying conditions of a vertical plate, atmospheric pressure, laminar flow and a film temperature (T_{film}) of 400K, the thermal resistance of and heat transfer through natural convection to air is calculated as follows:

$$\nu = 26.41 \times 10^{-6} m^2/s, \alpha = 38.3 \times 10^{-6} m^2/s, k_{air} = 33.8 \times 10^{-3} W/mK,$$

$$g = 9.81 m/s^2, C = 0.59, n = 1/4$$

$$Nu_L = \frac{h_L H}{k_{air}} = C(Ra_L)^n$$

$$Ra_L = \frac{g(\Delta T)H^3}{T_{film} \nu \alpha}$$

$$h_L = \frac{Ck_{air}(Ra_L)^n}{H} = 2.9593(\Delta T)^{1/4}$$

$$R_{air} = \frac{1}{h_L} = .3379(\Delta T)^{-1/4} [m^2K/W] \quad (31)$$

$$q_{air} = h_L A_s \Delta T = 1.4797 \times 10^{-3} (\Delta T)^{5/4} [W] \quad (32)$$

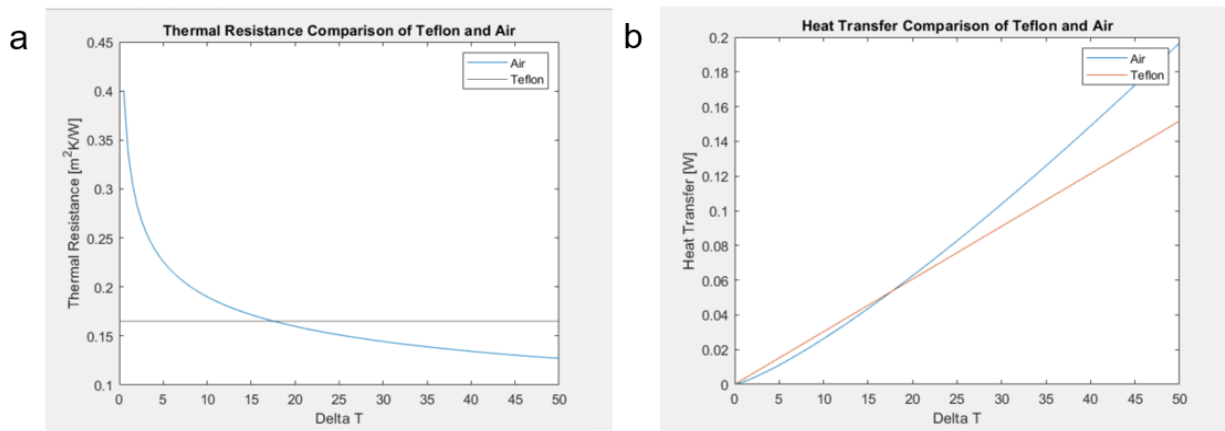


Figure 15: Teflon and air thermal performance comparison (a) Thermal resistance plot (b) Heat transfer plot

As depicted in Figure 16, for higher temperature differences, teflon has a greater thermal resistance and lower heat transfer. As a result, we decided to remove this pocket for complete PTFE coverage of the fin walls.

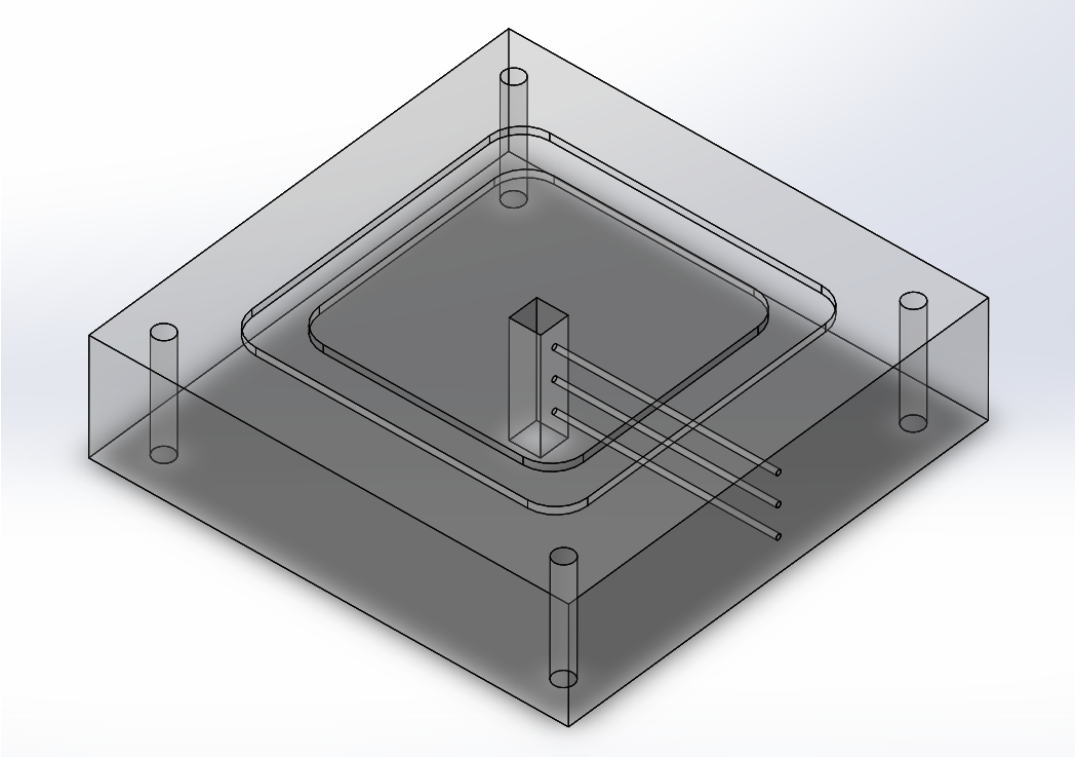


Figure 16: Upper base design

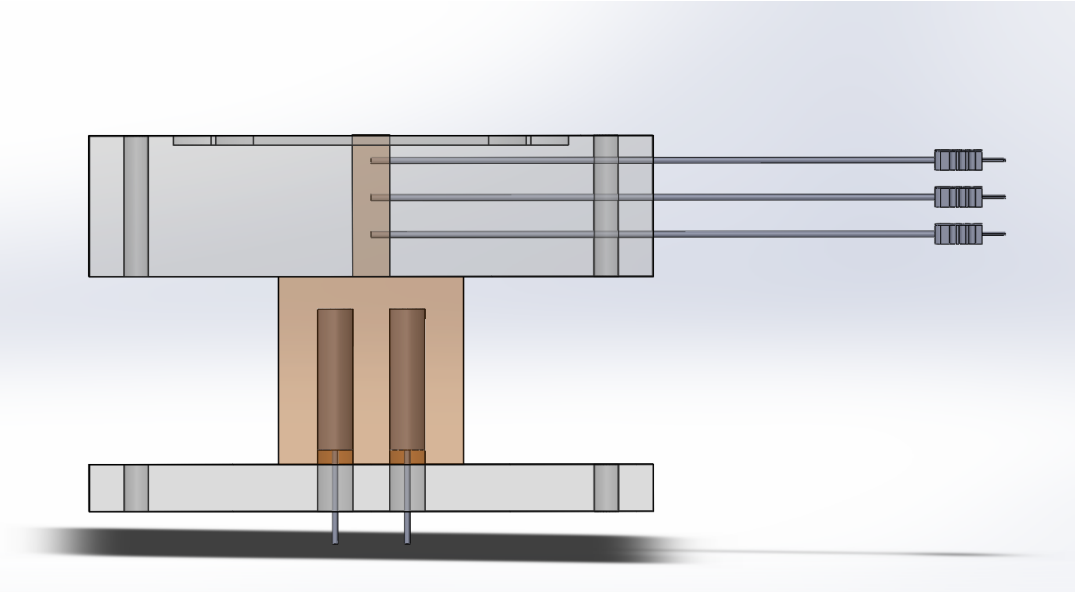


Figure 17: Side view of thermocouple hole alignment

In the lower base, four holes are machined to allow the cartridge heaters through into the heating block. From the previous setup design, we also eliminated an additional base that was around the cubical portion of the heating block for convenience and insulation purposes. In place of PTFE, fiberglass wool is thoroughly packed around the copper to promote one-dimensional thermal conduction to the boiling surface. Wool fiber has a significantly lower thermal conductivity than PTFE as well as can be easily removed when cooling down the system after tests. Fiber glass wool will also fill in the extra space below the cartridge heaters to further reduce heat loss.

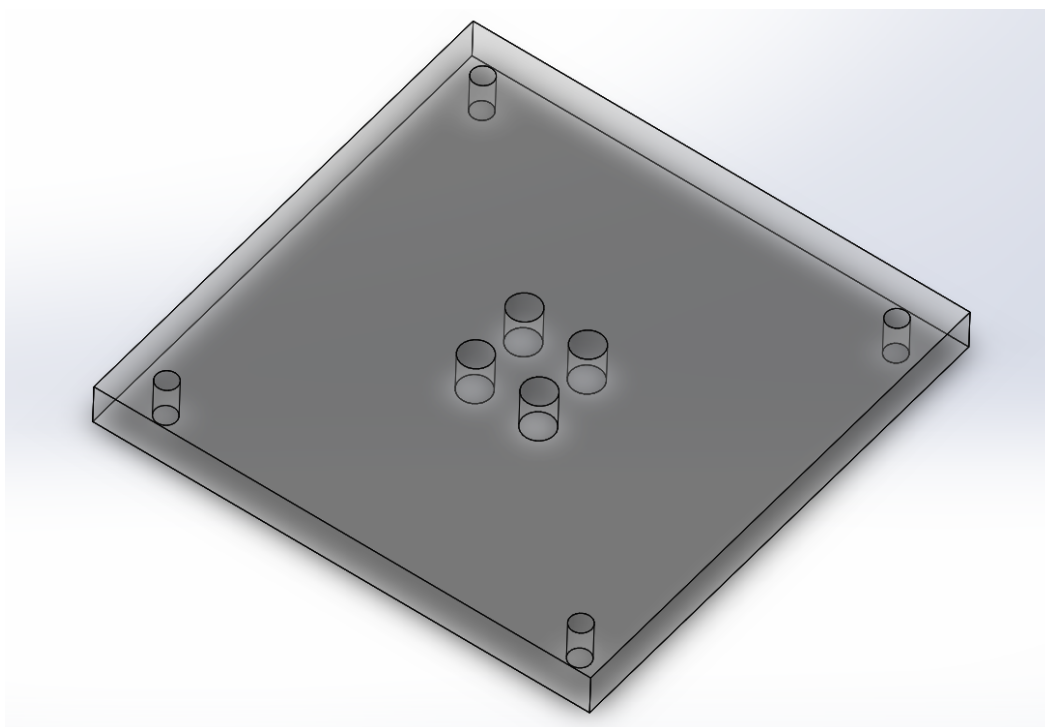


Figure 18: Lower base design

When designing our lid, we chose polycarbonate for its thermal as well as mechanical properties. Polycarbonate allows for easy machining of a shallow pocket to fit the second rubber gasket and through holes for adding and removing water, thermocouples, a condenser and an immersion heater. Tapered plugs are inserted into these holes to secure components in place and seal any gaps that could allow vapor to escape.

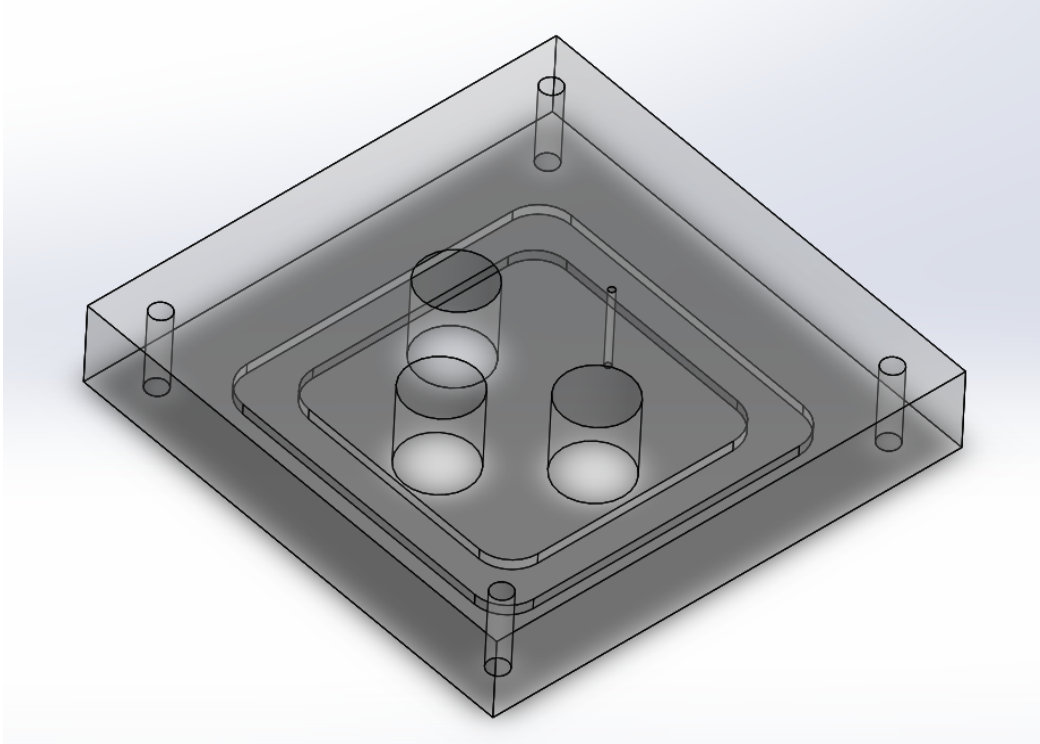


Figure 19: Lid design

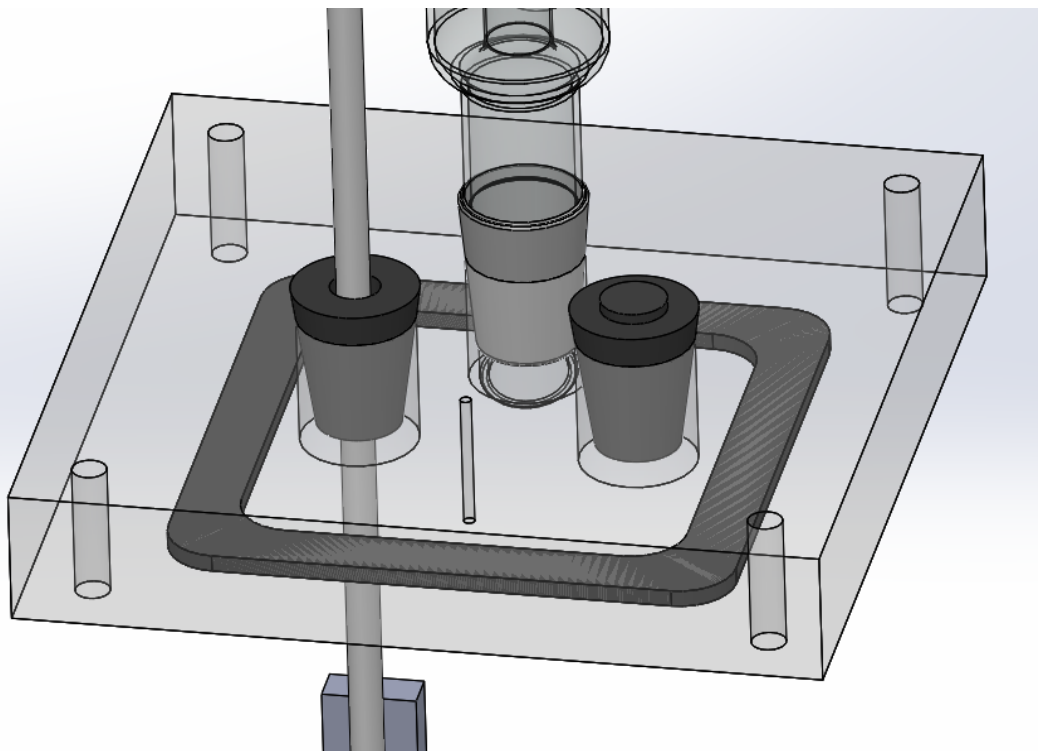


Figure 20: Lid assembly design

All these machined parts are then fastened together by four threaded bolts and held in the appropriate locations with hex screws and washers, displayed in figure 22.

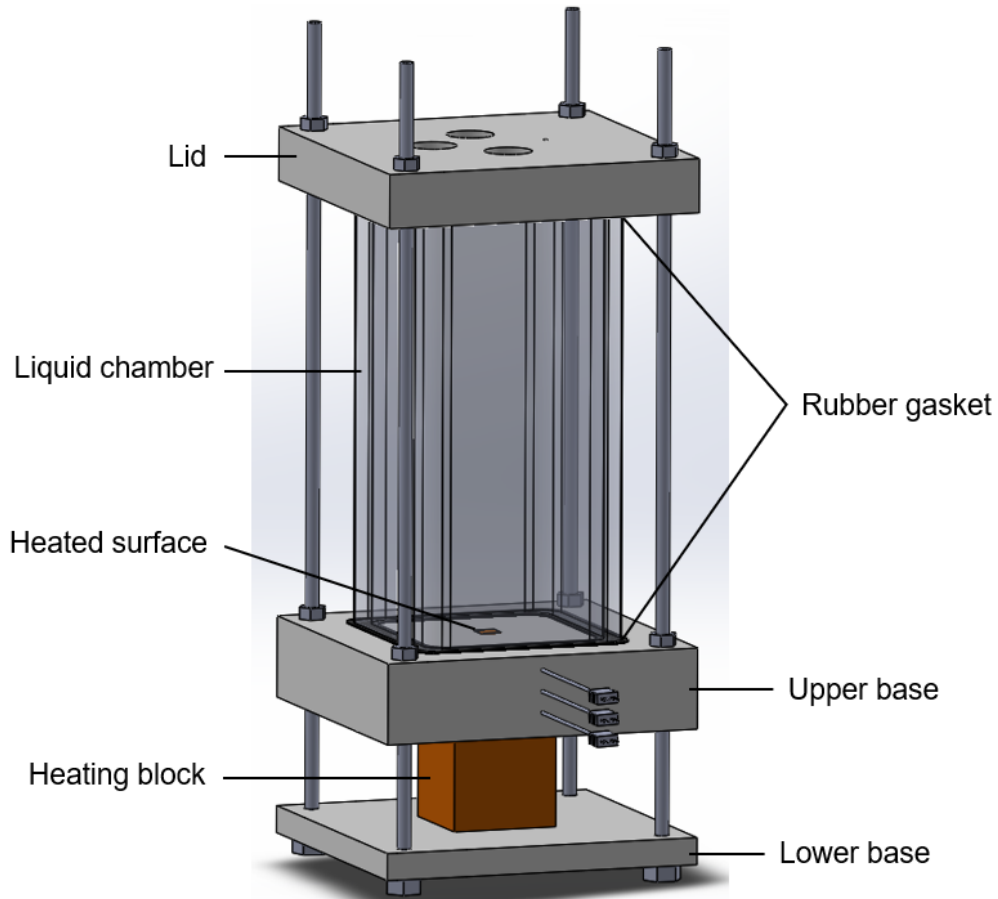


Figure 21: Pool boiling setup design assembly

3.2 Vendor Search

Once our pool boiling setup design was finalized, we began our search for vendors to create our main structural components; the heating block, upper base, lower base and lid. We had two options; (1) find one vendor that could provide both materials and machining services or (2) find separate vendors for materials and fabrication. The parameters considered in our decision-making were capabilities, lead time and price. Table 1 lays out these parameters for various vendors for option 1.

Company	Part/Material	Description/Comments	Lead Time (Weeks)	Price(\$)	Quantity
Xometry					
	Heating Block/Copper 101	+/- .002" tolerance	2	507.09	1
	Upper Base/PTFE	+/- .01" tolerance, International	2	402.43	1
	Lower Base/PTFE	+/- .01" tolerance, International	2	158.52	1
	Lid/Polycarbonate	+/- .01" tolerance, International	2	172.76	1
Plastic and Metal Center					
	Heating Block/Copper 101	+/- .002" tolerance	3	1,100	1
	Upper Base/PTFE	+/- .002" tolerance	3	1,750	1
	Lower Base/PTFE	+/- .002" tolerance	3	460	1
	Lid/Polycarbonate	+/- .002" tolerance	3	850	1
Sky Machine Inc					
	Heating Block/Copper 101	+/- .001" tolerance	3	485	1
	Upper Base/PTFE	+/- .002" tolerance	3	1,185	1
	Lower Base/PTFE	+/- .002" tolerance	3	435	1
	Lid /Polycarbonate	+/- .002" tolerance	3	485	1
Southern Copper and Supply Company					
	Heating Block/Copper 101	+/- .001" tolerance	4	435.05	1

Table 1: Material and fabrication vendor trade study

This option initially seemed ideal, as using a single vendor required less contact and middleman work on our end. However, with further investigation, we found that these services were either international, potentially leading to delays, or costly.

Now considering option 2, we began looking for separate material and fabrication vendors. Our first fabrication vendor of choice was that of UC Irvine's engineering department. Using our school's machine shop would enable easy communication with the machinist and therefore better guarantee the accuracy of our parts. We could provide parts, such as thermocouples and cartridge heaters, to ensure their designated holes were dimensioned and toleranced properly. Moreover, it would be assumedly quicker and cheaper than other vendors as we wouldn't have to ship materials/parts to and from. However, due to unique features of our design, there were additional tools that needed to be purchased; a #51 extra long drill bit for the thermocouple holes and a 10mmx10mm square broach for the square hole in the upper base. Although this increased the cost of our current project, these purchases were worthwhile as they can be reused for building future experimental setups. Table 2 details the UC Irvine machine shop's capabilities, cost and time estimates per part.

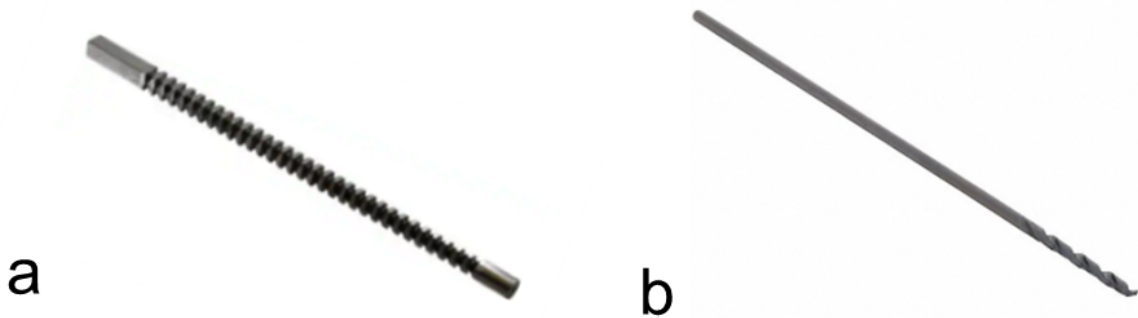


Figure 22: Additional machining tool purchases. (a) 10mm square broach (b) #51 extra long drill bit

UC Irvine Machine Shop	Part	Description/Comments	Machining Time(hr)	Price (\$)	Quantity
	Heating Block	+/- 0.002" tolerance, \$65/hr	3	195	1
	Upper Base	+/- 0.002" tolerance, \$65/hr	3	195	1
	Lower Base	+/- 0.002" tolerance, \$65/hr	1	65	1
	Lid	+/- 0.002" tolerance, \$65/hr	2	130	1

Table 2: UC Irvine machine shop estimates

Company	Part/Material	Description/Comments	Dimensions	Price(\$/ea)	Quantity
McMaster Carr					
	Upper Base/PTFE	+/- 0.25" tolerance	6"x6"x1.5"	163.33	2
	Lower Base/PTFE	+/- 0.25" tolerance	6"x6"x.5"	79.72	2
	Lid/Polycarbonate	+/- 0.5" tolerance	6"x12"x1"	228.56	1
Grainger					
	Upper Base/PTFE	+/- 1.0" tolerance	6"x6"x1.5"	150.14	2
	Lower Base/PTFE	+/- 0.5" tolerance	6"x6"x.5"	72.25	2
	Lid/Polycarbonate	+/- 0.25" tolerance	12"x12"x1"	348.58	1
EMCO Industrial Plastics					
	Upper Base/PTFE	+/- 0.060" tolerance	12"x18"x1.5"	1,448.70	1
	Lower Base/PTFE	+/- 0.060" tolerance	6"x12"x.5"	142.40	2
	Lid/Polycarbonate	+/- 0.060" tolerance	6"x18"x1"	218.63	1
Schorr					
	Heating block/Copper 101	N/A	2"x3"x4"	85	1
Southern Copper and Supply Company					
	Heating block/Copper 101	2": +/- .005" and 3.5" : +1/8", -0" tolerance	2"x2"x3.5"	75	1

Table 3: Material vendor trade study

The overall capabilities, time and cost of this option were deemed favorable but, before making a final decision, we needed to investigate material vendors. To point out, this trade study, shown in table 3, considers enough material for two pool boiling setups. After comparing tolerances, available dimensions, and prices, we decided on McMaster for PTFE and polycarbonate and Southern Copper and Supply Company for copper 101.

Combining the price of materials per setup and the UC Irvine machine shop services, it was clear that the second option was in fact more cost effective. Overall, taking this into account as well as the advantages previously described, we decided on option 2.

3.3 Subsystems Design

The main subsystems of our pool boiling setup are a reflux, heating source, temperature acquisition and visualization system. This section will discuss each of these system processes and the specific hardware components required for optimal performance.

3.3.1 Reflux System

For efficiency, we added a reflux condenser that enters the liquid chamber through the lid. This tool allows any non-condensable gasses to escape while also condensing vaporized working fluid and returning it to the system. The condensing process maintains the fluid level, reducing the need for continuous refiling as well as maintains atmospheric conditions inside the boiling chamber. After a comparative analysis of different condensers, we chose the dimroth condenser(24/40 Dimroth Condenser, Laboy Inc.). It's double spiral design with the coolant inlet and outlet both at the top provides maximum surface area and prevents clogging by having cooled water flow through the coil rather than around it. This addition will also result in a more consistent working fluid temperature, producing more accurate temperature readings. A water pump(3 Speed Circulation Pump, Tysun Inc.) is connected to the condenser's inlet and outlet joints with a hose to induce the flow of cooled water through the coil. This pump is also used to empty the liquid chamber once experiments are completed through the water inlet/outlet.

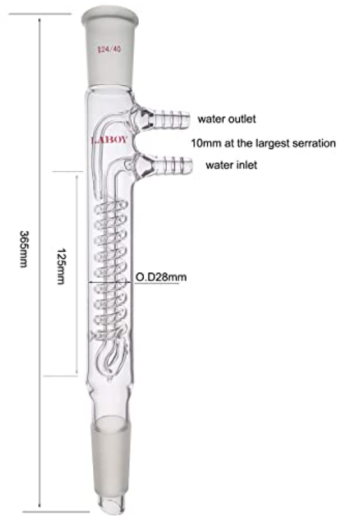


Figure 23: Reflux condenser(24/40 Dimroth Condenser, Laboy Inc.)



Figure 24: Water pump(3 Speed Circulation Pump, Tysun Inc.)

3.3.2 Heating Source System

Our main heating source consists of four cartridge heaters(CIR-20191/120V, Omega Inc.) snugly fit into cylindrical bored holes in the copper heating block. These cartridge heaters are connected to a power supply through an AC voltage regulator(Bench Top 20 Amp Variac Variable Auto-Transformer) to control the input power and therefore modulate the heat flux to the boiling surface. In order to maintain saturation conditions as well as degas the working fluid,

an immersion heater(120V portable water heater, Lewis N. Clark Inc.) is inserted through the lid. This is carried out by a PID controller(100V-220V Digital Thermostat Temperature PID Controller, Inkbird Inc) and solid state relay(40A SSR, Inkbird Inc.) that reads the water temperature and signals when to switch the immersion heater on and off. A smaller immersion heater with a shorter heated section allows for complete submersion into the water. As air and steam are still thermally conductive, this avoids overheating, reducing the risk of burning or even shattering our liquid chamber. In addition, before filling the liquid chamber, an electric kettle is used to preheat and initially degas the water.



Figure 25: Cartridge heater(CIR-20191/120V, Omega Inc.)



Figure 26: Immersion heater(120V portable water heater, Lewis N. Clark Inc.)



Figure 27: AC power supply(Bench Top 20 Amp Variac Variable Auto-Transformer)

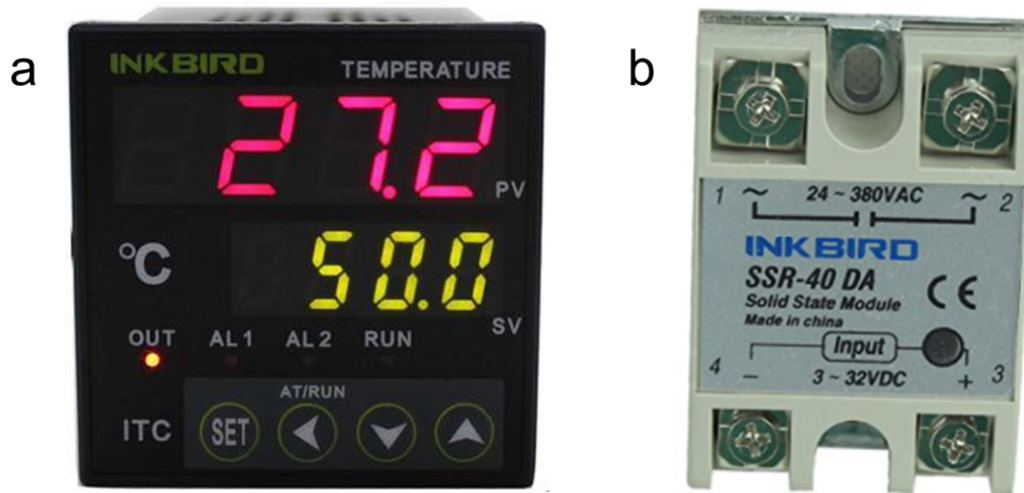


Figure 28: (a) PID controller(100V-220V Digital Thermostat Temperature PID Controller, Inkbird Inc.) (b) Solid state relay(40A SSR, Inkbird Inc.)

3.3.3 Temperature Acquisition System

To calculate the net heat flux and wall superheat, K-type thermocouples (TJ36-CASS-116U-6, Omega Inc.) were used and connected to a USB data acquisition(DAQ) system(U6, LabJack Inc.). This DAQ hardware is then connected to a computer where it records the temperature

readings from the thermocouples. Due to a smaller copper fin height, the number of thermocouple holes were reduced to three. These three K-type thermocouples read temperatures along the copper fin in the direction of heat conduction towards the boiling surface. To ensure good thermal contact between the thermocouple and the copper block, and therefore accurate temperature readings, thermal paste is applied to the probes before insertion. Another two sheathed thermocouples, connected to the LabJack and PID controller are inserted through the lid and submerged into the deionized water to measure and maintain saturation temperature.



Figure 29: K-type thermocouple(TJ36-CASS-116U-6, Omega Inc.)



Figure 30: USB data acquisition system(U6, LabJack Inc.)

3.3.4 Visualization System

For accurate bubble feature classification, it is essential to use clear, detailed images of our boiling experiments. To obtain such quality, recordings of bubble nucleation, growth and departure are taken with a high-speed camera(Mini AX50, FAST CAM Inc.) through one transparent side of the liquid chamber. In addition, an adjustable light(SugarCUBE LED fiber optic, The Ushio America Inc.) illuminates the backside of the chamber where a diffuser sheet is taped to evenly distribute background lighting.



Figure 31: High speed camera(Mini AX50, FAST CAM Inc.)



Figure 32: Adjustable light source (SugarCUBE LED fiber optic, The Ushio America Inc.)

3.4 Final Setup Assembly

All structural and subsystem designs are then integrated together as illustrated in both figure 34 and figure 35. Assembly of hardware components are properly wired and connected according to our schematic diagram in figure 35. Once the cartridge heaters and thermocouples are inserted, fiber glass wool is packed into the corresponding locations of the heating block. The experimental procedure is now ready to begin and will be explained in the following section.

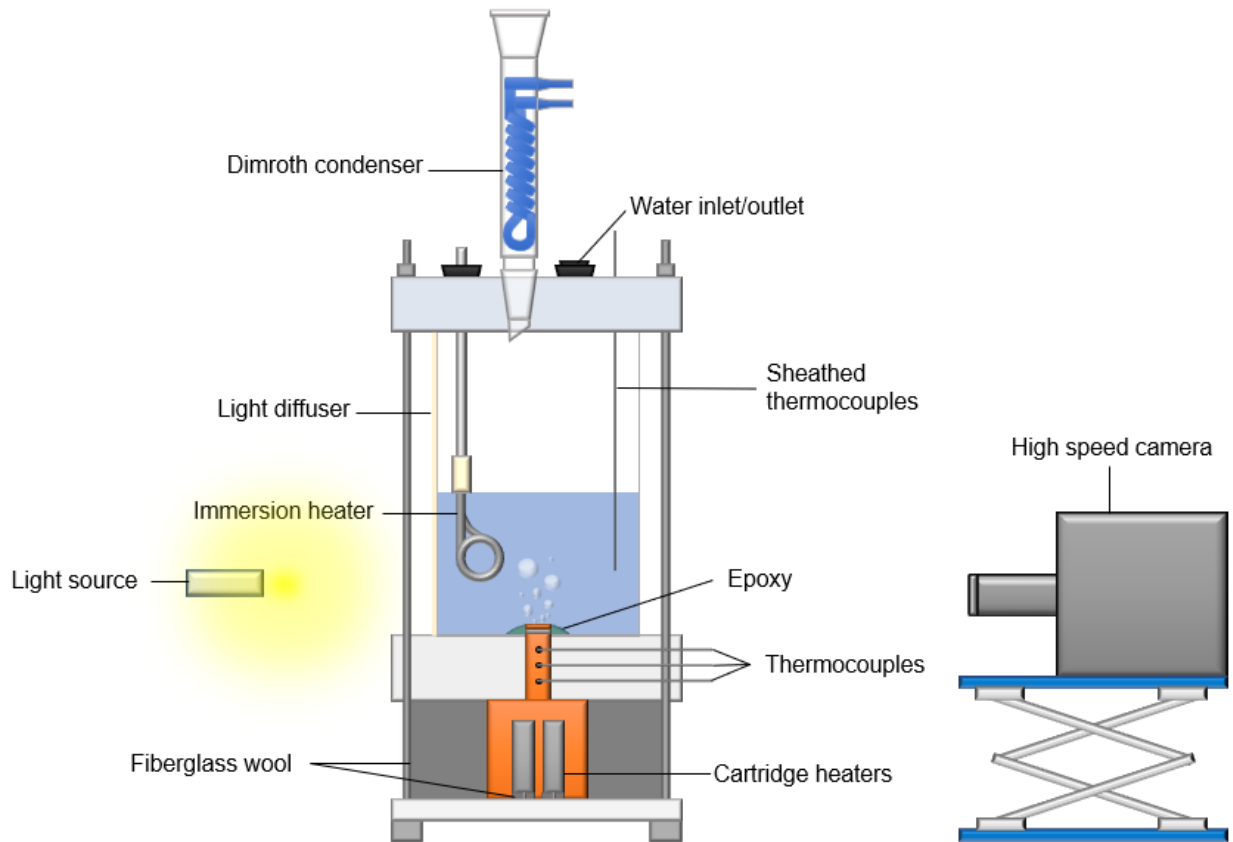


Figure 33. Pool boiling experimental setup components

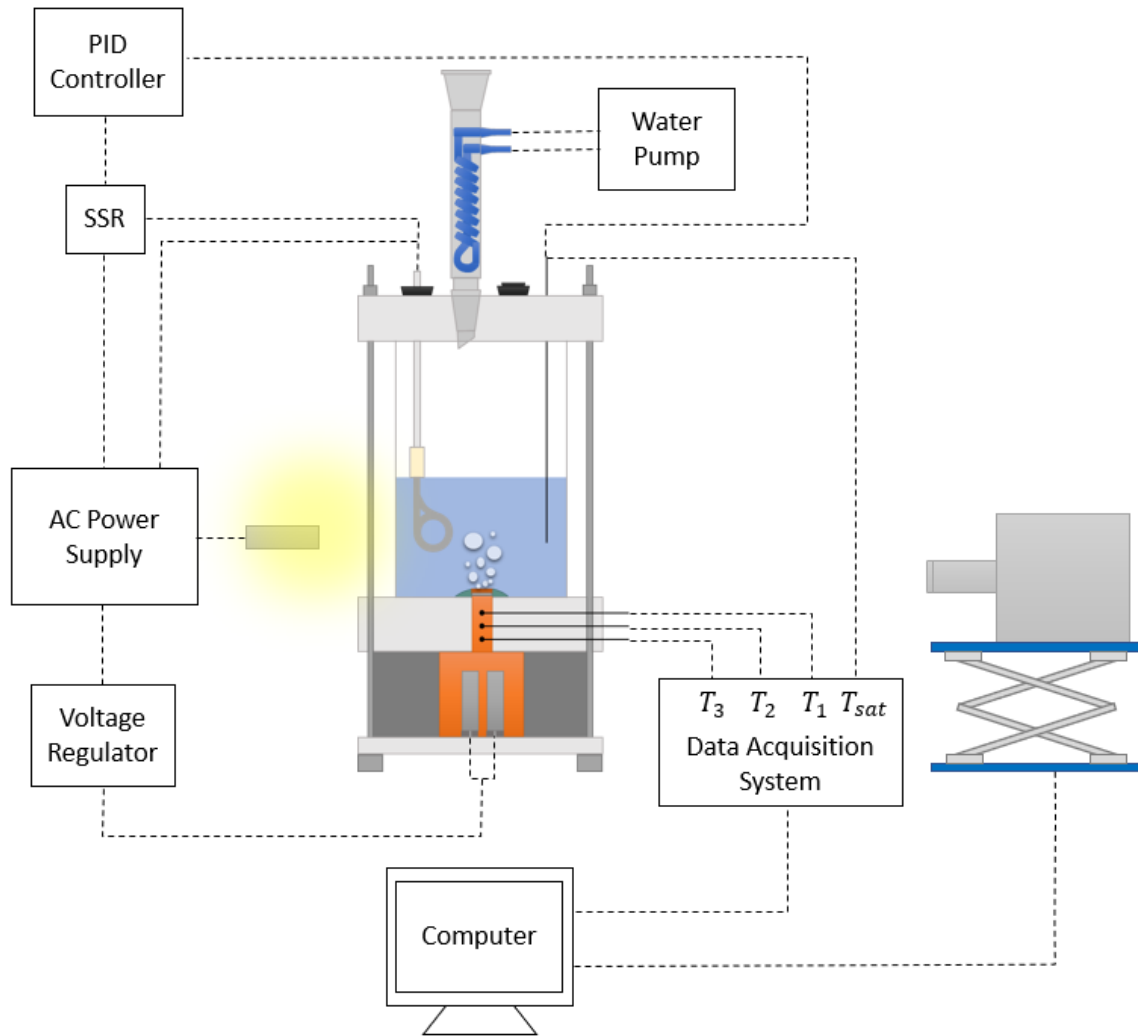


Figure 34: Schematic of pool boiling experimental setup

CHAPTER 4: EXPERIMENTAL METHODOLOGY

This chapter focuses on the pool boiling test procedure using our optimized set up as well as optimized image acquisition and thermal measurement methods. In addition, quantification of heat transfer performance from boiling statistics is discussed.

4.1 Sample Preparation

A 10mm x 10mm x 0.5mm piece of pure copper is cleansed for 5 minutes in a piranha solution. This is made of 3:1 mixture of sulfuric acid(H_2SO_4) and 30% Hydrogen Peroxide(H_2O_2) and removes any organic residues from the surface. The sample is then further cleansed with isopropyl alcohol and deionized water before mounting to the heated surface.

4.2 Sample Mounting

To achieve the same contact resistance between the sample and heating block and therefore obtain consistent results, we employ a meticulous sample mounting method. Once the surface is heated to the solder's melting point of about $180^\circ C$, we carry out a specific beading technique where a single bead or drop of solder paste is applied to the heated surface. Then, using cross-locking 90° angled tweezers, shown in figure 35a, we secure our copper sample, as illustrated in figure 35b. Holding our sample parallel to the surface, we lower it to the solder, applying a consistent pressure. This process reduces the chance of air pockets and ensures a .5mm thin and evenly distributed layer of solder between our heated surface and copper sample.

In previous experiments with the old setup, bubble nucleation surrounding the sample resulted in heat loss and obscured visualization of targeted bubble dynamics, depicted in figure 37. This also made it difficult when annotating to decipher which bubbles formed on the surface once

they departed. Therefore, prior to experiments, the sample is sealed with epoxy to prevent the escape of latent heat from its outer edges. Uneven application of epoxy also served as nucleation sites, further contributing to this issue. Thus, with our elevated heated surface we carefully create a smooth bond between the sample surface edges and the surrounding PTFE base.

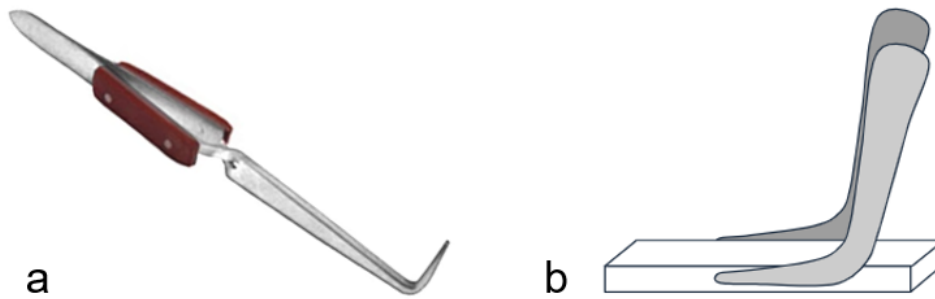


Figure 35: Sample mounting (a) 90° cross-locking tweezers (b) Mounting method Illustration

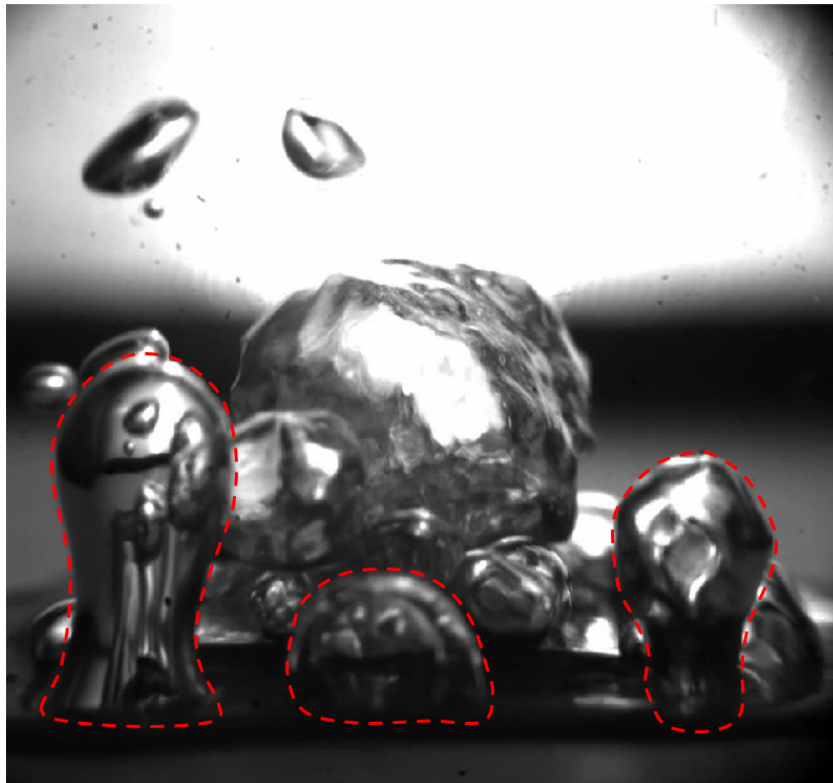


Figure 36: Obscured visualization from outer edge bubble nucleation

4.3 Setup Preparation and Clean up

Once the sample is mounted, the gaskets, liquid chamber and lid are secured in place. The reflux condenser and immersion heater are then inserted through the lid. The immersion heater is strategically held at a position to the side of the boiling surface and out of view of our high-speed camera view. Deionized water is preheated and degassed with an electric kettle then fed through the water inlet. The water level is maintained at the height of the heating section of our immersion heater to prevent overheating. Next, power is switched on to all components. The PID controller is configured to saturation temperature and cooled water is pumped through the condenser. The optimized setup is ready for data collection once the light source and high-speed camera are placed in their designated positions. Methods of our visualization and thermal measurement process are explained further in the next section.

After experiments are complete, power is shut off to all components. The fiberglass wool is carefully removed from the setup to begin cooling down our system. To quicken this process, a cool air dryer is directed towards the heated block. Finally, using the tubes and water pump from our reflux system, we drain our liquid chamber.

4.4 Image Acquisition

During pool boiling, bubbles rapidly explode from the surface in a volatile nature. Therefore, to ensure high quality images for accurate extraction of bubble features, we use an adjustable light source at the ideal setting as well as a light diffuser to minimize glare and harsh shadows. Positions of both the light source and high-speed camera are determined prior to data acquisition based on clarity of the live view. They are then clearly marked with tape for repeatable and consistent visual data across multiple test runs. Additionally, we set the resolution of our high-speed camera to 1024x1024 pixels at 2,000fps. Although high speed imaging lessens motion blur, it also produces datasets with very similar images. This puts more

weight on a small number of bubbles and impedes dataset diversity which can potentially introduce bias to the identification process. To avoid these issues, we employ randomized imaging, where for each heat flux step, images are captured at random time frames for a period of 30 seconds.

4.5 Thermal Measurement

This subsection explains the quantification of experimental heat transfer performance through thermocouple measurements. These temperatures are recorded until steady state is reached for each incrementally increased input heat load.

The net heat flux(q'') passing through the system, can be found using the one-dimensional Fourier's Law:

$$q'' = -k_{Cu} \frac{dT}{dX} \quad (33)$$

Where k_{Cu} is the thermal conductivity of copper $101(391.1W/mK)$ and $\frac{dT}{dX}$ is the temperature gradient, calculated by taking the average of $\frac{\Delta T_i}{\Delta X_{ij}}$ along the heat transfer direction. T_i represents the temperature readings from the three thermocouples and ΔX_{ij} represents the distance between each of these thermocouples. This results in the equation:

$$q'' = k_{Cu} \left[\frac{\left(\frac{T_1 - T_2}{\Delta X_{12}} \right) + \left(\frac{T_2 - T_3}{\Delta X_{23}} \right)}{2} \right] \quad (34)$$

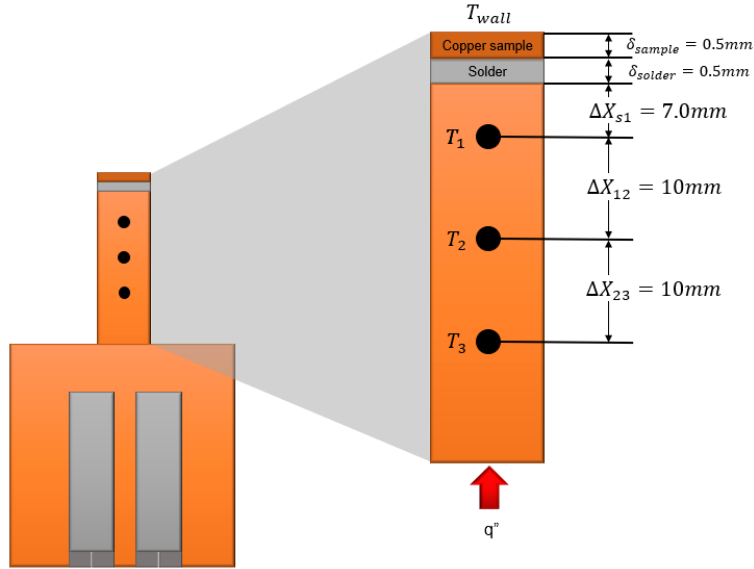


Figure 37: Schematic cross section of heating block fin with mounted sample

The surface temperature of the copper sample (T_{wall}) can be estimated using:

$$T_{wall} = T_1 - q'' \left(\frac{\Delta X_{s1}}{k_{Cu}} + \frac{\delta_{solder}}{k_{solder}} + \frac{\delta_{sample}}{k_{Cu}} \right) \quad (35)$$

Where ΔX_{s1} is the vertical distance between the first thermocouple and the top surface of the heating block, k_{solder} is the solder thermal conductivity ($\sim 50 W/mK$), and δ_{solder} and δ_{sample} is the thickness of the solder and copper sample, respectively.

To determine the boiling curve, the steady-state q'' is plotted against its corresponding wall superheat (ΔT), which is given by;

$$\Delta T = T_{wall} - T_{sat} \quad (36)$$

Then, the HTC can be found by relating the applied heat flux to the associated wall superheat, calculated with;

$$HTC = \frac{q''}{\Delta T_{wall}} \quad (37)$$

The uncertainty of the thermocouple measurements(U_T) is $\pm 1.1^\circ\text{C}$ and we assume that thermal conductivity remains constant and thermocouple position errors are minimized. Using the law of propagation of uncertainty for heat flux, which is as follows;

$$U_{q''} = \sqrt{\left(\frac{\partial q''}{\partial T_1} U_T\right)^2 + \left(\frac{\partial q''}{\partial T_2} U_T\right)^2 + \left(\frac{\partial q''}{\partial T_3} U_T\right)^2} \quad (38)$$

we approximate the maximum heat flux uncertainty as $\pm 3.04 \text{ W/cm}^2$.

4.6 Heat Flux Prediction Using Bubble Statistics

This subsection explains how the bubble statistics can be used to predict the corresponding heat flux. The predicted boiling heat flux to the surface can be found by summing the various heat transfer modes of natural convection(q''_{nc}), evaporation(q''_{ev}) and bubble departure forced convection(q''_{fc}) as follows:

$$q''_{tot} = q''_{nc} + q''_{fc} + q''_{ev} \quad (39)$$

Each heat transfer mode is governed by various boiling parameters, including the key bubble parameters of nucleation site density(N_b), bubble departure diameter(D_b), and bubble departure frequency(f_b). They can be calculated with the following equations [65][42]:

$$q''_{nc} = \left(1 - N_b \frac{\pi D_b^2}{4}\right) h_c \Delta T \quad (40)$$

$$q''_{fc} = \frac{1}{2} \left[D_b^2 N_b \left(\sqrt{\pi k \rho c f_b} \right) \Delta T \right] \quad (41)$$

$$q''_{ev} = N_b f_b \left(\frac{\pi}{6} D_b^3 \right) \rho_v h_{fg} \quad (42)$$

Where h_c is the average convective HTC outside of the area of influence that we define as

$h_c \approx .5 h_{exp}$ with h_{exp} as the experimentally measured HTC, ΔT is the superheat, ρ is the density

of the liquid, c is the heat capacity, and h_{fg} is the latent heat of evaporation [65]. This

methodology is then applied to the postprocessing module of our framework for autonomous heat flux predictions.

CHAPTER 5: SUMMARY AND CONCLUSION

This work presents an optimized pool boiling setup for maximized efficiency and reliability of experimental procedures. Its cutting edge design ensures accurate thermal data acquisition and enables real-time, high-resolution visualization of pool boiling processes. Traditional methods of extracting and interpreting data from pool boiling have proven invasive as well as operose; which in turn produces potentially biased and therefore questionable heat transfer correlations. However, with our machine learning-based computer vision model, we can autonomously track individual bubble features from massive datasets of pool boiling images to then extract higher-level features(e.g.,. active nucleation site density, bubble departure diameter, bubble departure frequency, heat flux, heat transfer coefficient). Unfortunately, even with the impressive performance of our vision-based machine learning approach, it is still difficult to precisely predict heat transfer performance solely from bubble statistics due to present simplified theoretical models. Nevertheless, the large bandwidth of accurately mined spatiotemporal bubble statistics can be used to fine-tune these models. Thus, future research will explore different pool boiling conditions such as enhanced surface and fluid properties to decipher the underlying mechanisms that impact the correlations between bubble dynamics and heat transfer performance. Furthermore, our optimized pool boiling setup design can be integrated into future studies involving different working fluids, surfaces or even visualization approaches such as top and bottom-views of bubble dynamics, adding another dimension to our mechanistic understanding of boiling physics. In conclusion, our proposed experimental setup and methodology in conjunction with our machine vision-based framework can help pave the way to discovering more effective cooling schemes for modern day thermal management systems.

REFERENCES

- [1] Moore, A. and Shi, L., 2014. Emerging challenges and materials for thermal management of electronics. *Materials Today*, 17(4), pp.163-174.
- [2] I. Mudawar, "Assessment of high-heat-flux thermal management schemes," *IEEE Transactions on Components and Packaging Technologies*, vol. 24, no. 2, pp. 122–141, 2001.
- [3] I. Mudawar, "Recent advances in high-flux, two-phase thermal management," *Journal of Thermal Science and Engineering Applications*, vol. 5, no. 2, 2013.
- [4] A. Bejan, "Pool Boiling Regimes," in *Convection Heat Transfer*, Hoboken, NJ: Wiley, 2013, pp. 447–451.
- [5] F. P. Incropera, "Boiling Modes," in *Fundamentals of heat and mass transfer*, Hoboken, NJ: J. Wiley, 2007, pp. 621–626.
- [6] G. Liang, Y. Chen, H. Yang, D. Li, and S. Shen, "Nucleate boiling heat transfer and critical heat flux (CHF) from micro-pit surfaces," *International Journal of Heat and Mass Transfer*, vol. 152, p. 119510, Feb. 2020.
- [7] N. Zuber, "Hydrodynamic aspects of boiling heat transfer (thesis)," thesis, United States Atomic Energy Commission, Technical Information Service, Washington, D.C., 1959.
- [8] G. Liang and I. Mudawar, "Review of Pool Boiling Enhancement with additives and nanofluids," *International Journal of Heat and Mass Transfer*, vol. 124, pp. 423–453, 2018.
- [9] H. Seo, Y. Lim, H. Shin, and I. C. Bang, "Effects of hole patterns on surface temperature distributions in pool boiling," *International Journal of Heat and Mass Transfer*, vol. 120, pp. 587–596, 2018.

- [10] G. Liang and I. Mudawar, "Review of pool boiling enhancement by surface modification," *International Journal of Heat and Mass Transfer*, vol. 128, pp. 892–933, 2018.
- [11] A. E. Bergles, R. L. Webb, G. H. Junkhan, and M. K. Jensen, "Bibliography on augmentation of convective heat and mass transfer," 1979.
- [12] R. Chen, M.-C. Lu, V. Srinivasan, Z. Wang, H. H. Cho, and A. Majumdar, "Nanowires for enhanced boiling heat transfer," *Nano Letters*, vol. 9, no. 2, pp. 548–553, 2009.
- [13] M. R. Hossain, M. I. Talukder, and M. A. Rahman, "Study of pool boiling on flat and micro-grooved brass and copper surfaces," *AIP Conference Proceedings*, 2019.
- [14] R. P. Rioux, E. C. Nolan, and C. H. Li, "A systematic study of pool boiling heat transfer on structured porous surfaces: From nanoscale through microscale to Macroscale," *AIP Advances*, vol. 4, no. 11, p. 117133, 2014.
- [15] S. J. Thiagarajan, R. Yang, C. King, and S. Narumanchi, "Bubble dynamics and nucleate pool boiling heat transfer on microporous copper surfaces," *International Journal of Heat and Mass Transfer*, vol. 89, pp. 1297–1315, 2015.
- [16] S. M. You, J. H. Kim, and K. H. Kim, "Effect of nanoparticles on critical heat flux of water in Pool Boiling Heat Transfer," *Applied Physics Letters*, vol. 83, no. 16, pp. 3374–3376, 2003.
- [17] J. Barber, D. Brutin, and L. Tadrist, "A review on boiling heat transfer enhancement with nanofluids," *Nanoscale Research Letters*, vol. 6, no. 1, 2011.
- [18] X. Kong, Y. Zhang, and J. Wei, "Experimental Study of Pool Boiling Heat transfer on novel bistructured surfaces based on micro-pin-finned structure," *Experimental Thermal and Fluid Science*, vol. 91, pp. 9–19, 2018.

- [19] G. Chen and C. H. Li, "Combined effects of liquid wicking and hydrodynamic instability on pool boiling critical heat flux by two-tier copper structures of nanowires and microgrooves," *International Journal of Heat and Mass Transfer*, vol. 129, pp. 1222–1231, 2019.
- [20] H. M. Kurihara and J. E. Myers, "The effects of superheat and surface roughness on boiling coefficients," *AIChE Journal*, vol. 6, no. 1, pp. 83–91, 1960.
- [21] G. Kocamustafaogullari and M. Ishii, "Interfacial area and nucleation site density in boiling systems," *International Journal of Heat and Mass Transfer*, vol. 26, no. 9, pp. 1377–1387, 1983.
- [22] R. J. Benjamin and A. R. Balakrishnan, "Nucleation site density in pool boiling of saturated pure liquids: Effect of surface microroughness and surface and liquid physical properties," *Experimental Thermal and Fluid Science*, vol. 15, no. 1, pp. 32–42, 1997.
- [23] N. Basu, G. R. Warrier, and V. K. Dhir, "Onset of nucleate boiling and active nucleation site density during subcooled flow boiling," *Journal of Heat Transfer*, vol. 124, no. 4, pp. 717–728, 2002.
- [24] S. R. Yang and R. H. Kim, "A mathematical model of the pool boiling nucleation site density in terms of the surface characteristics," *International Journal of Heat and Mass Transfer*, vol. 31, no. 6, pp. 1127–1135, 1988.
- [25] C. H. Wang and V. K. Dhir, "Effect of surface wettability on active nucleation site density during pool boiling of water on a vertical surface," *Journal of Heat Transfer*, vol. 115, no. 3, pp. 659–669, 1993.
- [26] S. Mori and Y. Utaka, "Critical heat flux enhancement by surface modification in a saturated pool boiling: A Review," *International Journal of Heat and Mass Transfer*, vol. 108, pp. 2534–2557, 2017.

- [27] A. Abdelhady, "Experimental Investigation of Pool Boiling and Boiling Under Submerged Impinging Jet of Nanofluids," thesis, 2013.
- [28] A. Ranjan, I. Ahmad, R. K. Gouda, M. Pathak, and M. K. Khan, "Enhancement of critical heat flux (CHF) in pool boiling with anodized copper surfaces," *International Journal of Thermal Sciences*, vol. 172, p. 107338, 2022.
- [29] J. Du, C. Zhao, and H. Bo, "A modified model for bubble growth rate and bubble departure diameter in nucleate pool boiling covering a wide range of pressures," *Applied Thermal Engineering*, vol. 145, pp. 407–415, 2018.
- [30] L. Z. Zeng, J. F. Klausner, and R. Mei, "A unified model for the prediction of bubble detachment diameters in boiling systems— I. Pool Boiling," *International Journal of Heat and Mass Transfer*, vol. 36, no. 9, pp. 2261–2270, 1993.
- [31] R. Cole, "Bubble frequencies and departure volumes at subatmospheric pressures," *AIChE Journal*, vol. 13, no. 4, pp. 779–783, 1967.
- [32] M. M. Mahmoud and T. G. Karayiannis, "Pool Boiling Review: Part I – Fundamentals of boiling and relation to surface design," *Thermal Science and Engineering Progress*, vol. 25, p. 101024, 2021.
- [33] M. Može, V. Vajc, M. Zupančič, R. Šulc, and I. Golobič, "Pool boiling performance of water and self-wetting fluids on hybrid functionalized aluminum surfaces," *Processes*, vol. 9, no. 6, p. 1058, 2021.
- [34] S. Hamzekhiani, M. M. Falahieh, M. R. Kamalizadeh, and Z. Nazari, "Experimental study on bubble departure frequency for pool boiling of water/nacl solutions," *Heat and Mass Transfer*, vol. 51, no. 9, pp. 1313–1320, 2015.

- [35] H. Chen, G. Chen, X. Zou, Y. Yao, and M. Gong, "Experimental investigations on bubble departure diameter and frequency of methane saturated nucleate pool boiling at four different pressures," *International Journal of Heat and Mass Transfer*, vol. 112, pp. 662–675, 2017.
- [36] R. Cole, "A photographic study of pool boiling in the region of the Critical Heat Flux," *AIChE Journal*, vol. 6, no. 4, pp. 533–538, 1960.
- [37] H. J. Ivey, "Relationships between bubble frequency, departure diameter and rise velocity in nucleate boiling," *International Journal of Heat and Mass Transfer*, vol. 10, no. 8, pp. 1023–1040, 1967.
- [38] L. Zhang, S. Gong, Z. Lu, P. Cheng, and E. N. Wang, "A unified relationship between bubble departure frequency and diameter during saturated nucleate pool boiling," *International Journal of Heat and Mass Transfer*, vol. 165, p. 120640, 2021.
- [39] J. H. Kim, "Enhancement of Pool Boiling Heat Transfer Using Thermally-Conductive Microporous Coating Techniques," Dissertation, 2006.
- [40] L. Dong, X. Quan, and P. Cheng, "An experimental investigation of enhanced pool boiling heat transfer from surfaces with micro/nano-structures," *International Journal of Heat and Mass Transfer*, vol. 71, pp. 189–196, 2014.
- [41] R. Bertossi, N. Caney, J. A. Gruss, J. Dijon, A. Fournier, and P. Marty, "Influence of carbon nanotubes on deionized water pool boiling performances," *Experimental Thermal and Fluid Science*, vol. 61, pp. 187–193, 2015.
- [42] N. Kurul and M. Z. Podowski, "Multidimensional effects in forced convection subcooled boiling," *Proceeding of International Heat Transfer Conference 9*, 1990.

- [43] R. J. Benjamin and A. R. Balakrishnan, "Nucleate pool boiling heat transfer of pure liquids at low to moderate heat fluxes," *International Journal of Heat and Mass Transfer*, vol. 39, no. 12, pp. 2495–2504, 1996.
- [44] M. Kim and S. J. Kim, "A mechanistic model for nucleate pool boiling including the effect of bubble coalescence on area fractions," *International Journal of Heat and Mass Transfer*, vol. 163, p. 120453, 2020.
- [45] Y. Suh, R. Bostanabad, and Y. Won, "Deep learning predicts boiling heat transfer," *Scientific Reports*, vol. 11, no. 1, 2021.
- [46] S. G. Kandlikar, "A theoretical model to predict pool boiling CHF incorporating effects of contact angle and orientation," *Journal of Heat Transfer*, vol. 123, no. 6, pp. 1071–1079, 2001.
- [47] V. K. Dhir, "Mechanistic prediction of nucleate boiling heat transfer—achievable or a hopeless task?," *Journal of Heat Transfer*, vol. 128, no. 1, pp. 1–12, 2005.
- [48] M. M. Petrovic and V. D. Stevanovic, "Coupled two-fluid flow and wall heat conduction modeling of nucleate pool boiling," *Numerical Heat Transfer, Part A: Applications*, pp. 1–29, 2021.
- [49] W. Nakayama, T. Daikoku, H. Kuwahara, and T. Nakajima, "Dynamic model of enhanced boiling heat transfer on porous surfaces—part I: Experimental investigation," *Journal of Heat Transfer*, vol. 102, no. 3, pp. 445–450, 1980.
- [50] W. Nakayama, T. Daikoku, H. Kuwahara, and T. Nakajima, "Dynamic model of enhanced boiling heat transfer on porous surfaces—part II: Analytical modeling," *Journal of Heat Transfer*, vol. 102, no. 3, pp. 451–456, 1980.

- [51] V. Serdyukov, I. Malakhov, and A. Surtaev, "High-speed visualization and image processing of sub-atmospheric water boiling on a transparent heater," *Journal of Visualization*, vol. 23, no. 5, pp. 873–884, 2020.
- [52] C. K. Yu and D. C. Lu, "Pool boiling heat transfer on horizontal rectangular fin array in saturated FC-72," *International Journal of Heat and Mass Transfer*, vol. 50, no. 17-18, pp. 3624–3637, 2007.
- [53] C.-D. Ghiu and Y. K. Joshi, "Visualization study of pool boiling from thin confined enhanced structures," *International Journal of Heat and Mass Transfer*, vol. 48, no. 21-22, pp. 4287–4299, 2005.
- [54] R. Pastuszko, "Pool boiling for extended surfaces with narrow tunnels – visualization and a simplified model," *Experimental Thermal and Fluid Science*, vol. 38, pp. 149–164, 2012.
- [55] G. M. Hobold and A. K. da Silva, "Machine learning classification of boiling regimes with low speed, direct and indirect visualization," *International Journal of Heat and Mass Transfer*, vol. 125, pp. 1296–1309, 2018.
- [56] G. M. Hobold and A. K. da Silva, "Visualization-based nucleate boiling heat flux quantification using machine learning," *International Journal of Heat and Mass Transfer*, vol. 134, pp. 511–520, 2019.
- [57] M. Ravichandran and M. Bucci, "Online, quasi-real-time analysis of high-resolution, infrared, boiling heat transfer investigations using artificial neural networks," *Applied Thermal Engineering*, vol. 163, p. 114357, 2019.

- [58] Y. Oktar, O. Ulucan, D. Karakaya, E. O. Ersoy, and M. Turkan, "Binocular vision based Convolutional Networks," *2020 28th Signal Processing and Communications Applications Conference (SIU)*, 2020.
- [59] A. F. Gad and C. Lin, *Shen du Xue Xi Ji Suan Ji Shi Jue Shi Zhan: Juan Ji Shen Jing Wang Luo, python, tensorflow he kivy*. Beijing: Qing hua da xue chu ban she, 2020.
- [60] A. N. Chernyavskiy and I. P. Malakhov, "CNN-based visual analysis to study local boiling characteristics," *Journal of Physics: Conference Series*, vol. 2119, no. 1, p. 012068, 2021.
- [61] A. Chatterjee, "Computational Investigation on Pool Boiling IR Images for Segmentation of Dry Spots Automatically and Evaluating the Performance of Traditional Image Processing and Deep Neural Networks in Quantifying Dry Area Segments," thesis, 2019.
- [62] G. M. Hobold and A. K. da Silva, "Automatic detection of the onset of film boiling using convolutional neural networks and Bayesian statistics," *International Journal of Heat and Mass Transfer*, vol. 134, pp. 262–270, 2019.
- [63] S. M. Rassoulinejad-Mousavi, F. Al-Hindawi, T. Soori, A. Rokoni, H. Yoon, H. Hu, T. Wu, and Y. Sun, "Deep Learning Strategies for critical heat flux detection in Pool Boiling," *Applied Thermal Engineering*, vol. 190, p. 116849, 2021.
- [64] H. Hessenkemper, S. Starke, Y. Atassi, T. Ziegenhein, and D. Lucas, "Bubble identification from images with machine learning methods," *TIVConsultancy*, Tempe, AZ, tech.
- [65] J. Lee, Y. Suh, M. Kuciej, P. Simadiris, M. Barako, and Y. Won, "Deep Vision-Inspired Bubble Dynamics on Hybrid Nanowires with Dual Wettability."

[66] A. Mikolajczyk and M. Grochowski, "Data augmentation for improving deep learning in image classification problem," *2018 International Interdisciplinary PhD Workshop (IIPhDW)*, 2018.

[67] T.-Y. Lin, M. Maire, S. Belongie, J. Hays, P. Perona, D. Ramanan, P. Dollár, and C. L. Zitnick, "Microsoft Coco: Common Objects in Context," *Computer Vision – ECCV 2014*, pp. 740–755, 2014.

[68] S. Visa; B. Ramsay; A. L. Ralescu; E. Van Der Knaap, *In Proceedings of the 22nd Midwest Artificial Intelligence and Cognitive Science (MAICS) Conference*, 2011, Cincinnati, Ohio, USA, 710, 120

[69] D. M. Powers, *arXiv preprint arXiv: 2010.16061* 2020